

See discussions, stats, and author profiles for this publication at: <https://www.researchgate.net/publication/349077964>

# An Adaptive Harmonic Polynomial Cell Method with Immersed Boundaries: Accuracy, Stability and Applications

Article in *International Journal for Numerical Methods in Engineering* · February 2021

DOI: 10.1002/nme.6648

CITATIONS

7

READS

212

4 authors:



**Chao Tong**

Technical University of Denmark

4 PUBLICATIONS 21 CITATIONS

[SEE PROFILE](#)



**Yanlin Shao**

Technical University of Denmark

65 PUBLICATIONS 531 CITATIONS

[SEE PROFILE](#)



**Harry B. Bingham**

Technical University of Denmark

113 PUBLICATIONS 2,410 CITATIONS

[SEE PROFILE](#)



**Finn-Christian Wickmann Hanssen**

Norwegian University of Science and Technology

17 PUBLICATIONS 101 CITATIONS

[SEE PROFILE](#)

Some of the authors of this publication are also working on these related projects:



Fully nonlinear simulation of freely-floating body motions [View project](#)



OES Task 10 [View project](#)

# An Adaptive Harmonic Polynomial Cell Method with Immersed Boundaries: Accuracy, Stability and Applications

Chao Tong<sup>1\*</sup>, Yanlin Shao<sup>1,2†</sup>, Harry B. Bingham<sup>1</sup>, Finn-Christian W. Hanssen<sup>3</sup>

1: Department of Mechanical Engineering, Technical University of Denmark, 2800, Lyngby, Denmark

2: College of Shipbuilding Engineering, Harbin Engineering University, 150001, Harbin, China

3: Centre for Autonomous Marine Operations and Systems (AMOS), Department of Marine Technology, N-7491, Trondheim, Norway

## Abstract

We present a 2D high-order and easily accessible immersed-boundary adaptive Harmonic Polynomial Cell (IB-AHPC) method to solve fully-nonlinear wave-structure interaction problems in marine hydrodynamics using potential-flow theory. To reduce the total number of cells without losing accuracy, adaptive quad-tree cell refinements are employed close to the free-surface and structure boundaries. The present method is simpler to implement than the existing IB-HPC alternatives, in that it uses standard square cells both in the fluid domain and at the boundaries, thus without having to use the more complex and expensive overlapping grids or irregular cells. The spurious force oscillations for moving structures, which is a known issue for immersed boundary methods (IBMs), are eliminated in this study by solving a separate boundary value problem (BVP) for a Lagrangian acceleration potential. We also demonstrate that solving a similar BVP for the corresponding Eulerian acceleration potential is far less satisfactory due to the involved second derivatives of the velocity potential in the body-boundary condition, which are very difficult to calculate accurately in an IBM-based approach. In addition, we present, perhaps for the first time since the HPC method was developed, a linear matrix-based stability analysis for the time-domain IB-AHPC method. The stability analysis is also used in this study as a general guide to design robust and stable numerical algorithms, in particular related to the treatment of boundary conditions close to the intersection between a Dirichlet and a Neumann boundary, which is essential in time-domain wave-structure interaction analyses using IBMs. We confirm theoretically through the stability analysis that square cells have the best stability properties. The present method has been verified and validated satisfactorily by various cases in marine hydrodynamics, including a moving structure in an infinite fluid, fully-nonlinear wave generation and propagation, and fully-nonlinear diffraction and radiation of a ship cross section.

**Keywords:** Harmonic Polynomial Cell method; Adaptive quad-tree cells; Potential flow; Immersed boundary method; Accuracy and stability analysis; Fully-nonlinear wave-body interaction

## 1 Introduction

Analysis of ships, and coastal and offshore structures, inevitably involves the modeling of water waves and their interaction with the structures. The natural physics of ocean flows can be well described by the Navier-Stokes (NS) equations with proper turbulence modeling [1, 2], using Computational Fluid Dynamics (CFD) methods. CFD can be expected to accurately capture the complicated flow details at small scales due to wave-structure interaction, in particular for physical processes such as wave breaking, turbulence, air entrapment and water jets. In the last decades,

---

\*Email address: ctong@mek.dtu.dk

†Email address: yshao@mek.dtu.dk

8 many CFD solvers have been developed and become widely used for various hydrodynamic stud-  
9 ies. Some of the CFD solvers are preferred in the scientific and engineering communities, such as  
10 open-source tools like OpenFOAM® [3, 4, 5] and REEF3D::CFD [6, 7], and commercial softwares  
11 like STAR-CCM+ [8] and ANSYS-FLUENT [9]. Development of highly accurate NS solvers are also  
12 attempted in recent years with success. Among others, a new staggered space–time discontinuous  
13 Galerkin method (DGM) has been proposed by Tavelli and Dumbser [10] to solve the NS equations,  
14 which was reported to reach arbitrary high order of accuracy both in time and space. More informa-  
15 tion on families of the staggered DGMs for solving the NS equations can be found in e.g. [11, 12, 13].  
16 Although a closer investigation of complex flows for wave-structure interaction can be achieved by  
17 these Navier-Stokes solvers, fine mesh resolution in the computational domain is required to fully  
18 capture the flow field. This makes them costly in terms of both CPU time and memory, which is  
19 the main bottleneck and challenge of applying CFD method for problems involving large-scale wave  
20 domains.

21 For large-volume marine structures, viscous effects are generally of secondary importance, and  
22 thus can be accounted for empirically as an engineering practice. It is therefore convenient and ideal  
23 to use potential-flow theory to predict the loading on, and response of, these structures [14, 15, 16].  
24 The conventional approach to model waves and wave-structure interaction within the context of  
25 potential flow is the Boundary Element Method (BEM) [17, 18, 19, 20, 21]. A high-order BEM was  
26 proposed in [18] to solve various strongly nonlinear wave problems like wave shoaling, run-up and  
27 plunging breakers. Among others, Ferrant et al. [19] and Bai and Eatock Taylor [22] applied BEMs  
28 to solve fully-nonlinear wave-structure interactions with success. Unlike other weakly-nonlinear ap-  
29 proaches based on perturbation schemes [23, 20], the exact fully-nonlinear free-surface boundary  
30 conditions are integrated in the time domain to update the wave profile and velocity potential on  
31 the instantaneous free surface. With  $N$  the number of unknowns on the boundaries of the computa-  
32 tional domain, a classical BEM takes  $O(N^2)$  operations to build up the influence coefficients for the  
33 discretized boundary integral equations. Solving the resulting dense-matrix equations takes CPU  
34 time proportional to  $O(N^3)$  for a direct method such as Gaussian-elimination or LU-factorization,  
35 and  $O(N^2)$  for an iterative solver. See the discussions in [24, 25]. This may lead to excessive CPU  
36 time for conventional BEMs, particularly for large-scale problems. On the other hand, thanks to  
37 the enhancement of BEMs, the operation complexity is notably reported to be reduced to  $O(N)$   
38 by using the fast multipole accelerated (FMA) method and  $O(N \log N)$  with pre-corrected FFT  
39 (pFFT) techniques [26, 27]. Another challenge for the application of BEMs is the corner problem  
40 at the wave-body intersection. Extra attention needs to be paid to Dirichlet-Neumann-boundary  
41 corners where the normal directions of the boundaries are discontinuous, otherwise it may lead to  
42 unstable solutions [28, 29]. This kind of problem can be effectively solved by either the double-node  
43 collocation techniques proposed by Grilli and Svendsen [29] and Tanizawa [30], or the multiple flux  
44 method by Hague and Swan [28].

45 In contrast to the BEM, field or volume methods discretize the entire fluid domain. Li and  
46 Fleming [31] originally applied a finite difference method (FDM) with a low-order multigrid technique  
47 to solve the Laplace equation for the fully-nonlinear potential-flow problems. Bingham and Zhang  
48 [32] further improved this model with a high-order finite difference scheme. This model was then  
49 extended to three dimensions, namely in the open-source code OceanWave3D by Engsig-Karup et  
50 al. [33] to study 3D nonlinear water waves with a flexible-order finite difference approximation.  
51 OceanWave3D was later enhanced with a GPU-based parallelization to increase the computational  
52 efficiency by Engsig-Karup et al. [34]. The finite element method (FEM) has also been successfully  
53 applied to study fully-nonlinear potential-flow problems. See for instance [35, 36, 37, 38]. A novel  
54 computational procedure to solve potential-flow problems is called the scaled boundary finite element

55 method (SBFEM). This method combines the advantages both from the FEM, that no fundamental  
56 solutions are required, and from the BEM, that the spatial dimension is reduced by one [39, 40, 41, 42].  
57 A coupled FEM and BEM can also be implemented to study wave-body interactions, where the FEM  
58 is used away from the body while the BEM is used in vicinity of the body (See, e.g. [43, 36]). The  
59 combination is based on consideration of the efficiency of FEM and BEM in computation and mesh  
60 generation, respectively.

61 Toward high accuracy and efficiency field methods for solving fully-nonlinear potential-flow prob-  
62 lems, a novel method, namely the Harmonic Polynomial Cell (HPC) method was proposed by Shao  
63 and Faltinsen [24] first in two dimensions (2D) and later extended to three dimensions (3D) by Shao  
64 and Faltinsen [44]. In recent years, many researchers have shown great interest in the application  
65 and further development of the HPC method. The local and global accuracy features of the 2D HPC  
66 method were investigated in depth by Ma et al. [45], who concluded that the local errors can be  
67 minimized by applying square-shaped cells. Bardazzi et al. [46] generalized the conventional 2D HPC  
68 method to solve the Poisson equation with success. The HPC solver combined with a viscous-flow  
69 solver through a domain-decomposition scheme was proposed by Hanssen [47] and Fredriksen et al.  
70 [48]. By doing so, in the region where the flow changes rapidly and viscosity cannot be neglected,  
71 the Navier-Stokes equations are applied, while in the bulk of the fluid the HPC method is used to  
72 dramatically reduce the computational time. The original HPC method, both in 2D and 3D, was  
73 developed based on boundary-fitted meshes, which makes it cumbersome for complex boundaries  
74 especially in 3D problems. Therefore, alternative techniques have been proposed to improve and  
75 enhance this method.

76 Hanssen et al. [49] and Zhu et al. [50] were the first to introduce the concept of the immersed  
77 boundary method (IBM) to the 2D HPC method. However, it was reported that the use of IBM  
78 can introduce spurious pressure oscillations for moving structures. To overcome this disadvantage,  
79 Hanssen et al. [51] and Hanssen [47] resorted to an overlapping-grid strategy, where a local grid  
80 attached to the structure overlaps with another global background grid. The local grid can be finer  
81 than the global grid to increase the accuracy of the solution. Since there is no relative motion between  
82 the body and the local grid, variation in the truncation errors at a moving surface introduced by an  
83 ordinary IBM are minimized, which also minimizes the spurious pressure oscillations. Very recently,  
84 Robaux and Benoit [52] also applied a similar overlapping-grid strategy in their development of a  
85 fully-nonlinear numerical wave tank based on the HPC method. Liang et al. [53] also applied the  
86 overlapping-grid to the free surface in a 3D HPC method for studying liquid sloshing in an upright  
87 circular tank. Tong et al. [54] used the method developed in Hanssen et al. [51] to systematically  
88 study the generation and interaction of solitary waves in a fully-nonlinear numerical wave tank.  
89 However, applying this overlapping-grid strategy involves two-way information exchange between  
90 the local and the global grids, which means that the size and topology of the global coefficient  
91 matrix changes with time. This is a disadvantage compared to using a boundary-fitted approach  
92 since the global coefficient matrix must be re-constructed at each time step. At the same time, for  
93 deep water and large wave domains, from an accuracy point of view, if square cells are adopted,  
94 the unknowns will dramatically increase, which increases the computational effort. Furthermore, as  
95 observed in Robaux and Benoit [52], instabilities on the free surface in the overlapping zone may  
96 occur due to reciprocal interpolation between two grid systems. To overcome this, Robaux and  
97 Benoit [52] proposed to use a free-surface relaxation between the local and global grids.

98 Another interesting development in the 2D HPC method was made recently by Wang et al. [25]  
99 and Shen et al. [55], where irregular cells close to the boundaries are constructed through a local  
100 approximation based on least-square fitting of harmonic polynomials. A similar idea was discussed  
101 by Shao and Faltinsen [44] in their formulation of the 3D HPC method. It also has similarities with

102 the weighted-least square (WLS) strategies applied in the FDM. An advantage of using irregular  
103 cells is that arbitrary order of polynomials could be included in the local approximations. With a  
104 proper free-surface tracking method, Wang et al. [25] have been able to deal with problems involving  
105 complex boundaries, i.e. plunging breakers, sloshing and water entry. However, a local irregular  
106 cell has to be formed for each boundary point at each time step in fully-nonlinear wave-structure  
107 interaction analysis, where the free surface and structure surfaces move or deform. Since a number  
108 of stencil points, typically much larger than that of a standard cell, are needed to form a solvable  
109 WLS problem, it can potentially increase the complexity and the computational cost of the method  
110 Shen et al. [55].

111 In the present study, we propose a new immersed-boundary HPC method, which avoids having  
112 to use the overlapping-grid strategy [51, 47, 52], or the irregular cells [25, 55] to handle complex  
113 geometries. As will be shown in later sections, the method has been satisfactorily verified and  
114 validated by several cases including: a circular cylinder moving in an infinite fluid where an analytical  
115 solution exists, fully-nonlinear wave generation and propagation, and fully-nonlinear diffraction and  
116 radiation of a ship cross section. The agreement with existing theoretical and experimental solutions  
117 demonstrate the satisfactory accuracy, stability and feasibility of the method.

118 The features and novelty of the present work are summarized as follows: Standard 4<sup>th</sup>-order  
119 square-shaped cells are consistently used both in the fluid domain and at the fluid boundaries so  
120 that no additional effort is needed to construct the local cells at each boundary node and each time  
121 step, since the interpolation coefficients of square cells are constant and easily scaled. Secondly,  
122 the cells are adaptively refined at the boundaries, either automatically or controlled by the user,  
123 to increase the accuracy where needed. This greatly reduces the number of unknowns to achieve a  
124 required accuracy; Thirdly, we show that the spurious force oscillations reported in the literature  
125 [49, 56, 47] for the IBM can be eliminated by solving a separate boundary value problem (BVP) for  
126 the Lagrangian acceleration potential. Another similar and widely used approach in fully-nonlinear  
127 potential-flow analysis, which solves the Eulerian acceleration potential, can reduce the force oscil-  
128 lations only if the grid close to the solid structure is fine enough. However, it does not eliminate  
129 the spurious force oscillations satisfactorily with an affordable cell resolution. This is related to the  
130 second derivatives of the velocity potential at the structure surface in the related BVP; Last but not  
131 least, we present, perhaps for the first time in the literature, a linear matrix-based stability analysis  
132 for the HPC method, which serves as a useful guide in the design of our numerical algorithms: includ-  
133 ing understanding the effect of the grid stretching and the proper treatment of Neumann boundaries  
134 to ensure the stability of the method.

135 The remainder of this paper is organized as follows. In § 2, the formulation of the potential-flow  
136 problem with fully-nonlinear boundary conditions is presented. § 3 outlines the basic theory about  
137 the HPC method, the IBM for free surfaces and body boundaries, and the Lagrangian acceleration  
138 potential method. In § 4 the grid system and the procedure of domain discretization are presented  
139 in detail. § 5 provides the validation of accuracy and spatial convergence for the numerical model,  
140 and a matrix-based stability analysis is also presented in this section. Three applications of this  
141 numerical model are given in § 6. In the end, § 7 summarizes the present work.

## 142 2 Fully nonlinear wave-structure interaction model

### 143 2.1 Governing equation and boundary conditions

144 A 2D Cartesian coordinate system  $Oxz$  is defined with its origin fixed at the middle of a numerical  
 145 wave tank, the  $Ox$  axis coinciding with the undisturbed free surface and  $Oz$  axis orienting positively  
 146 upward, as shown in Fig. 1. By applying potential-flow theory, the fluid is assumed to be ideal,  
 147 without viscosity. The flow is considered as irrotational and the fluid is incompressible. The fluid  
 148 motion in the domain  $\Omega$  can then be described by a velocity potential  $\varphi(x, z)$ , which satisfies the  
 149 Laplace equation:

$$\frac{\partial^2 \varphi}{\partial x^2} + \frac{\partial^2 \varphi}{\partial z^2} = 0, \quad \text{in } \Omega_{\text{fluid}}. \quad (1)$$

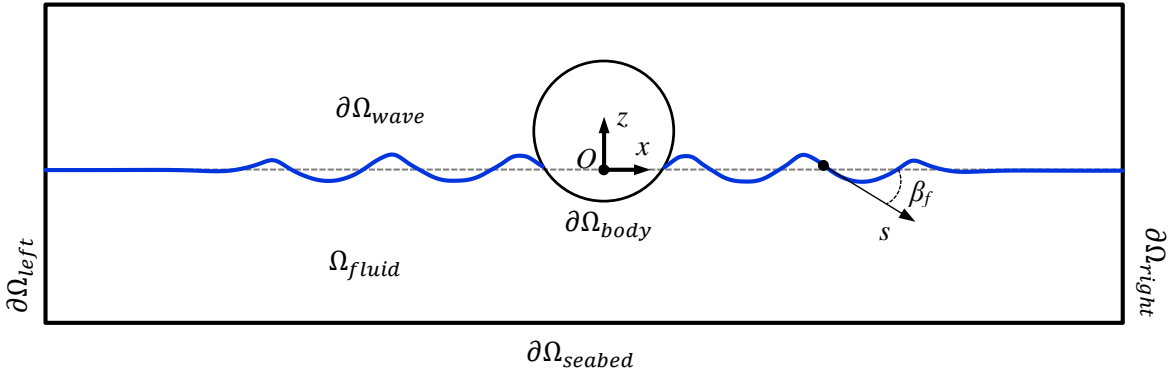


Figure 1: Sketch of wave-body interaction model in a numerical wave tank.

150 Along  $\partial\Omega_{\text{wave}}$ , the coordinates of a point on the free surface are denoted as  $(x(t), \eta(x, t))$  in the  
 151 inertial reference frame. The free-surface boundary conditions in the inertial reference frame are  
 152 expressed by the Lagrangian time derivative  $\delta/\delta t = \partial/\partial t + \mathbf{v} \cdot \nabla$  as:

$$\begin{cases} \frac{\delta x}{\delta t} = \frac{\partial \varphi}{\partial x} + (\mathbf{v} - \nabla \varphi) \cdot \nabla x, \\ \frac{\delta \eta}{\delta t} = \frac{\partial \varphi}{\partial z} + (\mathbf{v} - \nabla \varphi) \cdot \nabla \eta - \nu(x)\eta, \end{cases} \quad \text{on } \partial\Omega_{\text{wave}}, \quad (2)$$

$$\frac{\delta \varphi}{\delta t} = -\frac{1}{2} |\nabla \varphi|^2 - g\eta + \mathbf{v} \cdot \nabla \varphi - \nu(x)\varphi, \quad \text{on } \partial\Omega_{\text{wave}}, \quad (3)$$

153 where  $g$  is the gravitational acceleration,  $\nabla x = (1, 0)$  and  $\nabla \eta = (\partial \eta / \partial x, 0)$ . Here  $\mathbf{v} = 0$  corresponds  
 154 to an Eulerian description, while  $\mathbf{v} = \nabla \varphi$  corresponds to the fully Lagrangian description and  
 155  $\mathbf{v} = (0, \partial \eta / \partial t)$  gives a semi-Lagrangian description.  $\nu(x)$  is a damping coefficient which is only active  
 156 in the wave-absorbing zone and is zero elsewhere. In Eq. (3),  $\partial \varphi / \partial t = -\frac{1}{2} |\nabla \varphi|^2 - g\eta$  is derived from  
 157 Bernoulli's equation where the water pressure on the free surface is equal to the constant atmospheric  
 158 pressure. The fully-nonlinear free surface conditions are integrated forward in time using the explicit  
 159 4<sup>th</sup>-order Runge-Kutta scheme.

160 The fluid domain is enclosed by either Dirichlet boundaries  $\Gamma_D$  or Neumann boundaries  $\Gamma_N$ . In  
 161 order to solve the Laplace equation, Dirichlet and Neumann boundary conditions are needed and  
 162 given as:

$$\varphi(x, z) = \varphi_D, \quad \text{on } \Gamma_D, \quad (4)$$

$$\frac{\partial \varphi(x, z)}{\partial n} = \nabla \varphi \cdot \mathbf{n}, \quad \text{on } \Gamma_N, \quad (5)$$

163 where  $\mathbf{n}$  denotes the unit normal vector on Neumann boundaries pointing into the fluid domain. On  
 164 the Neumann boundaries, the fluid cannot penetrate the body surface so that the right-hand side  
 165 of Eq. (5) equals the normal velocity of the body boundary. For a numerical wave tank, Dirichlet  
 166 boundary conditions are imposed on the free surface. The right-hand side of Eq. (4) comes from the  
 167 time integration of the dynamic boundary condition on the free surface in Eq. (3). For a wave-body  
 168 interaction problem, a mixed Dirichlet-Neumann boundary value problem (BVP) will be solved for  
 169 the velocity potential at each time step.

## 170 2.2 Wave-body surface intersection problem

171 The intersection of the wave-body surface can cause numerical problems due to the discontinuity  
 172 of flux, if one does not properly take care of this. Proper treatment of the intersection point is not  
 173 only of significant importance to the global accuracy and stability of the numerical solution, but also  
 174 critical to the prediction of wave run-up along the body surface and the loads on floating structures.  
 175 To make sure that the intersection point remains on both the body surface and the free surface  
 176 during the time integration, Liu et al. [57] provided a velocity formula at the intersection point to  
 177 accomplish this goal. Tanizawa [30] used a double-node technique to deal with the discontinuity of  
 178 flux at the intersection point for the BEM. Hague and Swan [28] proposed a multiple flux BEM to  
 179 replace the double-node collocation with a single node to be placed at the intersection point. This  
 180 method was proven to be more accurate than the double-node techniques for wave propagation and  
 181 wave-body interactions.

182 In this paper, the velocity of the wave-body intersection point on the free surface is transformed  
 183 from a Cartesian coordinate system into a curvilinear coordinate system:

$$\begin{cases} \frac{\partial \varphi_f}{\partial x} = \frac{\partial \varphi_f}{\partial s} \cos \beta_f - \frac{\partial \varphi_f}{\partial n} \sin \beta_f, \\ \frac{\partial \varphi_f}{\partial z} = \frac{\partial \varphi_f}{\partial s} \sin \beta_f + \frac{\partial \varphi_f}{\partial n} \cos \beta_f, \end{cases} \quad (6)$$

184 where  $\beta_f \in (-\frac{\pi}{2}, \frac{\pi}{2})$  is the angle between the  $s$ - and the  $x$ -axis, defined clockwise positive. As shown  
 185 in Fig. 1, the  $s$ -axis coincides with the tangential direction to the free surface pointing in the positive  
 186 direction of the  $x$ -axis, and  $\beta_f$  can be determined by

$$\beta_f = \arctan\left(-\frac{\partial \eta}{\partial x}\right). \quad (7)$$

187 Here  $\partial \eta / \partial x$  is the slope of the free surface, which will be obtained in this study by a cubic spline  
 188 fitting. In order to deal with the flux discontinuity at the intersection point, we will follow the  
 189 approach by Grilli and Svendsen [29] to modify the tangential velocity  $\partial \varphi_f / \partial s$  in Eq. (6) as:

$$\frac{\partial\varphi_f}{\partial s} = \frac{\partial\varphi_b}{\partial n} \cdot \frac{1}{\sin(\beta_f - \beta_b)} - \frac{\partial\varphi_f}{\partial n} \cdot \frac{1}{\tan(\beta_f - \beta_b)}, \quad (8)$$

190 where  $\partial\varphi_b/\partial n$  and  $\partial\varphi_f/\partial n$  are the normal velocities at the intersection point to the body surface  
 191 and the free surface, respectively.  $\beta_b$  is defined as the angle between the normal vector to the body  
 192 surface and the  $z$ -axis. If the angle is defined positive in a clockwise direction, then  $\beta_b = \pi/2$  at left  
 193 tank wall and  $\beta_b = 3\pi/2$  at right tank wall.

## 194 3 The Harmonic Polynomial Cell (HPC) method with im- 195 mersed boundaries

### 196 3.1 The original HPC method in 2D

197 The HPC method was originally proposed by Shao and Falinsen [24] to solve potential-flow prob-  
 198 lems. Due to the property of high accuracy and efficiency, more and more attention is being paid to  
 199 this novel method by both the research and the engineering communities. In our present study, unlike  
 200 the 'irregular cells' strategy in Wang et al. [25], square cells are used in the whole computational  
 201 domain. Since the HPC method is a field solver, the computational domain is, therefore, discretized  
 202 into overlapping quadrilateral cells with local indices  $i = 1 \sim 9$ , as shown in Fig. 2. The origin of  
 203 the local coordinate system  $O\xi\zeta$  is located at the central point of each cell. The main idea of the  
 204 HPC method is to approximate the velocity potential  $\varphi(\xi, \zeta)$  by a linear weighted superposition of  
 205 the first eight harmonic polynomials within a cell, in a matrix form as:

$$\varphi(\xi, \zeta) = \sum_{j=1}^8 b_j p_j(\xi, \zeta) \implies \varphi(\xi, \zeta) = \mathbf{p}(\xi, \zeta) \cdot \mathbf{b} \quad (9)$$

206 where  $\mathbf{p} = [p_1(\xi, \zeta), p_2(\xi, \zeta), \dots, p_8(\xi, \zeta)]$ .  $p_j(\xi, \zeta)$ , ( $j = 1, 2, \dots, 8$ ) is either the real or the imaginary  
 207 part of the complex  $n$ -th order harmonic polynomial from  $(\xi + i\zeta)^n = \mathbf{u}(\xi, \zeta) + i\mathbf{v}(\xi, \zeta)$ . Here  $i = \sqrt{-1}$ ,  
 208 and  $\mathbf{b} = [b_1, b_2, \dots, b_8]^T$  is the weighted coefficient vector. The first eight harmonic polynomials are  
 209 listed in Table. 1. After inserting the local coordinates  $(\xi_i, \zeta_i)$ , ( $i = 1, 2, \dots, 8$ ) of the border nodes  
 210 into Eq. (9):

$$\begin{bmatrix} p_1(\xi_1, \zeta_1) & \cdots & p_8(\xi_1, \zeta_1) \\ \vdots & p_j(\xi_i, \zeta_i) & \vdots \\ p_1(\xi_8, \zeta_8) & \cdots & p_8(\xi_8, \zeta_8) \end{bmatrix} \cdot \begin{bmatrix} b_1 \\ \vdots \\ b_j \\ \vdots \\ b_8 \end{bmatrix} = \begin{bmatrix} \varphi_1 \\ \vdots \\ \varphi_i \\ \vdots \\ \varphi_8 \end{bmatrix} \implies \mathcal{P}\mathbf{b} = \boldsymbol{\varphi}, \quad (10)$$

211 the unknown coefficients  $b_j$  ( $j = 1, 2, \dots, 8$ ) in vector  $\mathbf{b}$  can be resolved as:

$$\mathbf{b} = \mathcal{C}\boldsymbol{\varphi}, \quad (11)$$

212 where matrix  $\mathcal{C}$  (with elements  $c_{j,i}$  ( $j, i = 1, 2, \dots, 8$ )) is the inverse of the matrix  $\mathcal{P}$ , whose elements  
 213 are  $p_{i,j} = p_j(\xi_i, \zeta_i)$ , ( $j, i = 1, 2, \dots, 8$ ). Note that both matrices  $\mathcal{P}$  and  $\mathcal{C}$  are only dependent on the  
 214 cell geometry. Therefore, they are constant if the cell does not change. Substituting Eq. (11) into  
 215 the interpolation equation (9) yields

$$\varphi(\xi, \zeta) = \mathbf{p}(\xi, \zeta) \cdot \mathcal{C}\boldsymbol{\varphi}. \quad (12)$$

216 Eq. (12) indicates that the potential at any point within a cell can be approximated by the linear  
 217 combination of the velocity potential on the eight border nodes of the cell. One could make an  
 218 analogy of this approximation to a finite difference or node-based finite element approximation. The  
 219 connectivity equation for the velocity potential in the fluid domain is obtained by inserting the local  
 220 coordinates of the central point  $i = 9$  into Eq. (12):

$$\varphi_9 = \varphi(0, 0) = \mathbf{c} \cdot \boldsymbol{\varphi}. \quad (13)$$

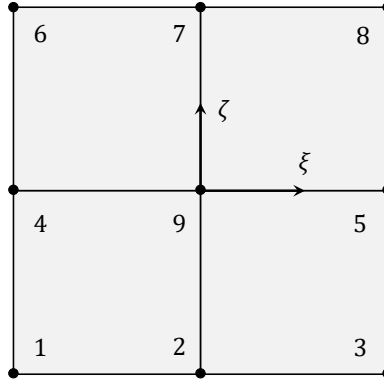


Figure 2: Sketch of a cell with local indices and coordinate system.

221 Here  $\mathbf{c}$ ,  $(c_{1,i}, i = 1, 2, \dots, 8)$  is the first row of matrix  $\mathcal{C}$ . As Eq. (12) serves as Dirichlet boundary  
 222 conditions, and Eq. (13) is applied for inner fluid nodes, then on the solid boundaries, the normal  
 223 derivative of the velocity potential involved in the Neumann boundary condition is obtained by  
 224 directly taking the normal derivative of the harmonic polynomials:

$$\frac{\partial \varphi}{\partial n}(\xi, \zeta) = \mathbf{q}(\xi, \zeta) \cdot \mathcal{C}\boldsymbol{\varphi}, \quad (14)$$

225 where the element of the vector  $\mathbf{q}(\xi, \zeta)$  is defined as  $q_j(\xi, \zeta) = \nabla p_j(\xi, \zeta) \cdot \mathbf{n}(\xi, \zeta)$ ,  $(j = 1, 2, \dots, 8)$ .  
 226 Here,  $\mathbf{n}(\xi, \zeta)$  is the normal vector on the boundary. Since the harmonic polynomials automatically  
 227 satisfy the Laplace equation, imposing the Laplace equation numerically becomes unnecessary in  
 228 this case. This feature is a natural advantage for the HPC method compared to other potential-flow  
 229 field solvers. In theory, the accuracy of the HPC method can reach arbitrary orders as long as high-  
 230 order harmonic polynomials are utilized. In this case, the cell can be changed into irregular shapes  
 231 containing the necessary number of nodes to reach a desired accuracy [44, 25]. Establishing the  
 232 adequate equations for all active nodes in the computational domain, the linear algebraic equation  
 233 system is established as  $\mathcal{A}\boldsymbol{\varphi} = \mathbf{e}$ , with  $\mathcal{A}$  the coefficient matrix containing at most nine entries in  
 234 each row,  $\boldsymbol{\varphi}$  the unknown velocity-potential vector and  $\mathbf{e}$  the boundary-condition vector.

### 235 3.2 Free surface and structure geometry modelled as immersed bound- 236 aries

237 As generation of body-fitted grids could be cumbersome for structures with complex and/or  
 238 moving geometry, the immersed boundary method (IBM) was proposed and implemented to make it  
 239 easy to deal with arbitrary geometries in regular grids. Hanssen et al. [49] first introduced the IBM  
 240 technique to the HPC method for a moving rigid body in an infinite fluid domain. Later on, Hanssen

Table 1: List of harmonic polynomials categorized into real and imaginary part of  $(\xi + i\zeta)^n$ .

| $n$ | $\mathbf{u}(\xi, \zeta)$                            | $\mathbf{v}(\xi, \zeta)$                  |
|-----|---|---|
| 0   | $p_1(\xi, \zeta) = 1$                               | -   |
| 1   | $p_2(\xi, \zeta) = \xi$                             | $p_3(\xi, \zeta) = \zeta$                 |
| 2   | $p_4(\xi, \zeta) = \xi^2 - \zeta^2$                 | $p_5(\xi, \zeta) = \xi\zeta$              |
| 3   | $p_6(\xi, \zeta) = \xi^3 - 3\xi\zeta^2$             | $p_7(\xi, \zeta) = 3\xi^2\zeta - \zeta^3$ |
| 4   | $p_8(\xi, \zeta) = \xi^4 - 6\xi^2\zeta^2 + \zeta^4$ | -   |

241 et al. [51] enhanced this idea to the free surface in a numerical wave tank and proved that this  
 242 method works well for various wave propagation problems, such as solitary waves in shallow water,  
 243 focused waves and periodic waves in shallow and deep water. Moreover, Hanssen [47] successfully  
 244 treated both the free surface and the body surface as immersed boundaries at the same time to study  
 245 fully-nonlinear wave-body interaction. In the work by Hanssen et al. [49], spurious force oscillations  
 246 were observed when the structure moves relative to the fixed grid. The main reason for these spurious  
 247 oscillations was that the time derivative of the velocity potential, needed to compute the pressure in  
 248 Bernoulli's equation, was estimated using backward finite difference. By instead solving a separate  
 249 BVP for the time derivative of the velocity potential in [47], the spurious pressure oscillations are  
 250 avoided. Hanssen et al. [51] and Hanssen [47] introduced overlapping, structured grids following the  
 251 motion of the moving bodies. This was mainly done in order to refine the solution locally, but it  
 252 also eased the formulation of the body-boundary condition in the BVP for the time derivative of the  
 253 velocity potential. An IBM to refine the grid locally without using overlapping grids, while avoiding  
 254 spurious pressure oscillations, will be discussed in detail in the following sections.

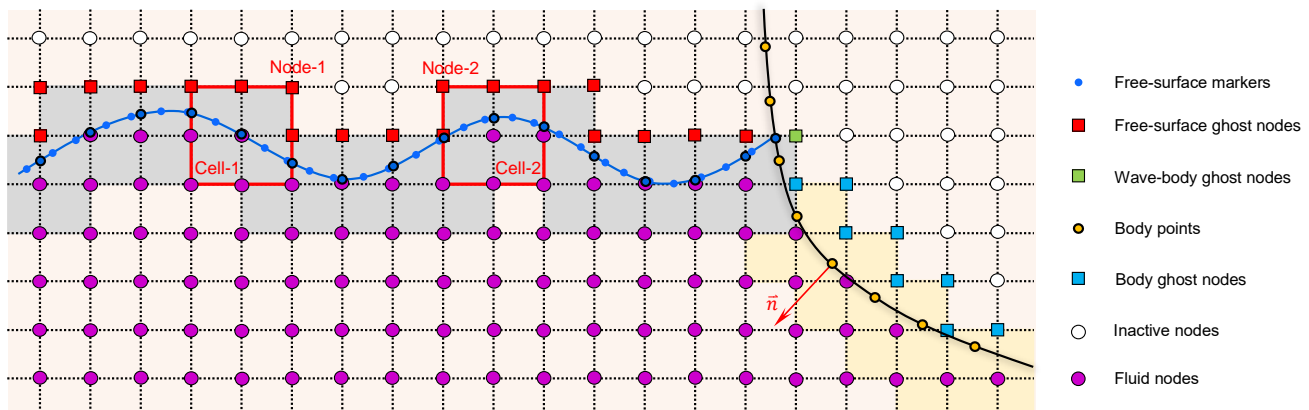


Figure 3: Immersed boundary method for free surface and body geometry. The free surface in a structured Cartesian grid is tracked by markers, and the body surface is represented by body points. The cells shaded in gray are used to impose free-surface conditions, while the cells shaded in yellow are used to impose Neumann boundary conditions.

255 Fig. 3 shows the free surface and body boundary modelled as immersed boundaries. The free  
 256 surface is discretized with a set of *wave markers* (blue circles with or without a black edge), and the  
 257 body is represented by a set of discrete points (yellow circles with a black edge). All the node types  
 258 are defined in Fig. 3. For the interior fluid nodes, the connectivity equation (13) will be applied  
 259 to ensure the continuity of the velocity potential and its time derivative across the fluid domain.

260 To impose Dirichlet boundary conditions on the free surface, the velocity potential on the *wave*  
261 *markers* will be interpolated using a proper cell, which always contains ghost nodes in its border  
262 nodes. The selected cells for the wave markers will be referred as *free-surface cells* in this paper.  
263 Two different types of *wave markers*, namely the semi-Lagrangian and fully Lagrangian markers, are  
264 defined. Fully Lagrangian markers are only used close to the body surface, while semi-Lagrangian  
265 wave markers are used elsewhere on the free surface. The semi-Lagrangian *wave markers* (blue circles  
266 with a black edge excluding the one on the body boundary) are only allowed to move along vertical  
267 grid lines. They are always within certain *free-surface cells*, where the markers are located on the  
268 upper half of the vertical central lines of the cells. The fully Lagrangian *wave markers* (blue circles  
269 without a black edge) are free to move horizontally and vertically, following the material velocity  
270 of the water particles. A cell will be associated to a Lagrangian *wave marker*, if the following two  
271 conditions are met: (1) The marker is located at the upper part of the cell; (2) Among other neighbor  
272 cells, the marker is closest to the vertical central line of the selected cell. Then this marker is defined  
273 to be an active marker. This principle of selecting the *free-surface cells* is inspired by the observation  
274 in [45] that the interpolation accuracy along the middle lines of the harmonic polynomial cells is the  
275 best. Referring to Fig. 2, the nodes with local index-7 in a *free-surface cell* will be denoted as a  
276 *free-surface ghost node*. If we denote the coordinates of an active marker as  $(\xi_m, \zeta_m)$  in the local cell  
277 coordinate system, the Dirichlet free-surface boundary condition is imposed as

$$\mathbf{p}(\xi_m, \zeta_m) \cdot \mathcal{C}\varphi = \varphi_m, \quad (15)$$

278 where  $\varphi_m$  is the velocity potential on the *wave maker*. Here, both the coordinates  $(\xi_m, \zeta_m)$  and the  
279 velocity potential  $\varphi_m$  of a wave marker can be directly obtained by time-integration of the free-surface  
280 conditions in Eq. (2) and (3), respectively. Meanwhile, matrix  $\mathcal{C}$  is determined once the geometry of  
281 the cell is fixed and  $\mathbf{p}(\xi_m, \zeta_m)$  can also be calculated if the coordinates  $(\xi_m, \zeta_m)$  of a wave marker are  
282 known, so that Eq. (15) can be accounted for in the global matrix system with only the unknowns  
283 velocity potential  $\varphi$  on border nodes of a cell to be resolved. In general, the number of active *wave*  
284 *markers* should be the same as that of the *free-surface ghost nodes*. If there is more than one ghost  
285 node on a cell border, called *additional free-surface ghost nodes*, see Node-1 and Node-2 in Cell-1 and  
286 Cell-2 respectively in Fig. 3 for example, then *extra wave makers* will be created on the free surface  
287 by interpolating the wave elevation and velocity potential from other *wave makers*. A cubic B-spline  
288 interpolation is used for this purpose. Generally, this *extra wave maker* is below the *additional free-*  
289 *surface ghost node* and coincides with the intersection point of the free surface and the vertical grid  
290 line where the *additional free-surface ghost node* is located on. In summary, the number of Dirichlet  
291 free-surface boundary condition equations is same as that of ghost nodes above the free surface.

292 As for the body boundary condition, *body ghost nodes* and *body cells* have to be identified first.  
293 If a grid node is inside the body, and at least one of its eight surrounding grid nodes are outside the  
294 body, it will be labeled as a *body ghost node*. A *body cell* should contain part of the body boundary,  
295 and its border nodes should not include any inactive nodes. Similar to what we have done for the  
296 *wave markers*, the Neumann boundary condition at a *body marker* (denoted as body nodes in Fig. 3)  
297 will be imposed using the interpolation from the corresponding *body cell*. The total number of *body*  
298 *ghost nodes* should be the same as that of the *body markers*. Therefore, for each *body ghost node*,  
299 a *body marker* closest to this ghost node will be created on the body surface, and its coordinates  
300 and normal direction are obtained by using a cubic B-spline interpolation. In practice, we always  
301 use high resolution of body markers to describe the body geometry to ensure we can extract more  
302 precise interpolation values from it. If we denote the coordinates of a *body marker* as  $(\xi_b, \zeta_b)$  in the  
303 local cell coordinate system, and the corresponding rigid-body velocity at this point is  $\mathbf{V}$ , then the

304 body boundary condition is imposed as

$$\mathbf{q}(\xi_b, \zeta_b) \cdot \mathcal{C}\varphi = \frac{\partial\varphi}{\partial n}(\xi_b, \zeta_b) = \mathbf{V} \cdot \mathbf{n}. \quad (16)$$

305 where  $\mathbf{n}$  is the unit normal vector at the corresponding *body marker* pointing into fluid.

306 As seen in Fig. 3, there is a special ghost node marked in green with a black edge, called the  
 307 *wave-body ghost node*. For this kind of node, since it is associated with the intersection between  
 308 the free surface and body surface (waterline point), special treatment is needed to ensure stability.  
 309 As we will show later in the stability analysis for a time-domain wave-making problem, imposing a  
 310 Neumann boundary condition at the waterline provides a more stable solution. The difference from  
 311 Eq. (16) is that it will share the information from the intersection point. Since the location of the  
 312 waterline point is obtained based on the free surface conditions, we get the boundary condition by  
 313 inserting the coordinates  $(\xi_m, \zeta_m)$  of the wave marker at the intersection point into Eq. (16) yielding

$$\mathbf{q}(\xi_m, \zeta_m) \cdot \mathcal{C}\varphi = \mathbf{V} \cdot \mathbf{n}, \quad (17)$$

314 while the velocity and normal vector from body movement at the intersection point are still applied.

### 315 3.3 The Lagrangian acceleration potential method

316 The instantaneous pressure on the body surface can be computed from Bernoulli's equation:

$$P = -\rho(\varphi_t + \frac{1}{2}|\nabla\varphi|^2 + gz). \quad (18)$$

317 Integrating the pressure over the wetted body surface yields the hydrodynamic forces  $\mathbf{F}_{hydro}$  and  
 318 moments  $\mathbf{M}_{hydro}$  on the body:

$$\mathbf{F}_{hydro} = - \int_{\Gamma_S} P \mathbf{n} ds, \quad \mathbf{M}_{hydro} = - \int_{\Gamma_S} P \mathbf{r} \times \mathbf{n} ds. \quad (19)$$

319 where  $\mathbf{n}$  is the normal vector pointing into the fluid. In order to get  $\mathbf{F}_{hydro}$  and  $\mathbf{M}_{hydro}$ , it is  
 320 necessary to calculate the time derivative of the velocity potential  $\varphi_t$ , also called the acceleration  
 321 potential. The direct way to compute  $\varphi_t$  is by a backward finite-difference in time, which however  
 322 has been proven to cause unexpected spurious oscillations in the time series of forces when the  
 323 IBM is applied to a moving body [49, 56, 47]. Note that the spurious oscillation is not due to the  
 324 known instability (see e.g. [58, 59]) related to the body motion equations, as it occurs even for  
 325 forced oscillation problems. To avoid the instability associated with the equations of body motion,  
 326 the Eulerian acceleration potential method (EAPM) has been proposed and also applied by many  
 327 researchers [60, 58, 61, 59, 62]. We denote it as EAPM since an Eulerian description is implied in  
 328 this approach. This approach has been proven to be very useful in improving accuracy and stability  
 329 in prediction of large-amplitude motions of floating structures [63]. Since  $\varphi_t$  also satisfies the Laplace  
 330 equation, i.e.  $\nabla^2\varphi_t = 0$ , it can be computed by solving another boundary value problem (BVP) in  
 331 the same way as that for the velocity potential. The corresponding body-boundary condition is given  
 332 as:

$$\frac{\partial\varphi_t}{\partial n} = (\dot{\mathbf{U}}_c + \dot{\boldsymbol{\omega}}_c \times \mathbf{r}) \cdot \mathbf{n} + (\boldsymbol{\omega}_c \times \mathbf{n}) \cdot (\mathbf{U}_c - \nabla\varphi) - (\mathbf{U}_c + \boldsymbol{\omega}_c \times \mathbf{r}) \cdot (\mathbf{n} \cdot \nabla)\nabla\varphi, \quad (20)$$

333 where  $\dot{\mathbf{U}}_c$  is the translational acceleration of the moving body and  $\dot{\boldsymbol{\omega}}_c$  is the angular acceleration  
 334 about the rotation center. More details on the derivation of this equation can be found in [59, 62].

335 The last term in Eq. (20), associated with the second derivatives of the velocity potential, can  
 336 be difficult to compute accurately. As it will be shown later, when the IBM is used, EAPM still  
 337 introduces spurious oscillations, and it is not better than a backward finite-difference.

338 Alternatively, a method solving a BVP for a Lagrangian acceleration potential, proposed and  
 339 applied by [64] and [65], seems to work very well. We will hereafter call it the Lagrangian acceleration  
 340 potential method (LAPM). According to [64], we could define the following generalized material  
 341 derivative of the velocity potential as:

$$\Psi = \frac{\delta\varphi}{\delta t} = \frac{\partial\varphi}{\partial t} + \mathbf{V} \cdot \nabla\varphi, \quad (21)$$

342 where  $\delta\varphi/\delta t$  denotes the time derivative of  $\varphi$  following a point that moves with the rigid-body velocity  
 343  $\mathbf{V} = \mathbf{U}_c + \boldsymbol{\omega}_c \times \mathbf{r}$ . Greco [65] proved that  $\Psi(x, z, t)$  is a harmonic function which means

$$\nabla^2\Psi = 0, \quad (22)$$

344 so that we can define a BVP for  $\Psi$  in the same way as the velocity potential, referred to in  
 345 Eqs. (12)~(14). On the free surface, the Dirichlet boundary condition is given as:

$$\Psi = \mathbf{V} \cdot \nabla\varphi - \frac{1}{2}|\nabla\varphi|^2 - g\eta. \quad (23)$$

346 At a moving body surface, the impermeable condition reads  $\partial\varphi/\partial n = \mathbf{V} \cdot \mathbf{n}$ . Meanwhile, according  
 347 to [65], the following relation holds for  $\Psi$

$$\frac{\partial\Psi}{\partial n} = \frac{\partial}{\partial n} \left( \frac{\delta\varphi}{\delta t} \right) = \frac{\delta}{\delta t} \left( \frac{\partial\varphi}{\partial n} \right) = \frac{\delta}{\delta t} (\mathbf{V} \cdot \mathbf{n}). \quad (24)$$

348 Using the operator  $\delta/\delta t = \partial/\partial t + \mathbf{V} \cdot \nabla$  yields

$$\frac{\partial\Psi}{\partial n} = \dot{\mathbf{V}} \cdot \mathbf{n} + \mathbf{V} \cdot (\boldsymbol{\omega}_c \times \mathbf{n}). \quad (25)$$

349 By direct comparison, this boundary condition for  $\Psi$  is simpler than that for the Eulerian acceleration  
 350 potential in Eq. (20). In contrast to Eq. (20), Eq. (25) does not involve any derivatives of the velocity  
 351 potential. This can significantly improve the accuracy of the calculation when using the IBM for a  
 352 moving body. After the BVP for  $\Psi$  is solved, we can obtain the the time derivative of the velocity  
 353 potential by  $\varphi_t = \Psi - \mathbf{V} \cdot \nabla\varphi$ . It should be noted that this method can be applied not only to a  
 354 rigid body but also to a flexible body. More details can be found in [66].

## 355 4 Adaptive Cartesian grid system

356 It has been shown, by Ma et al. [45], that the use of distorted cells in the 2D HPC method  
 357 can compromise the global accuracy of the solver. As a general rule, square cells ensure the highest  
 358 accuracy. In order to accurately model the rapid flow change near body boundaries or the free surface  
 359 solely using square cells, local grid refinement is adopted in our study. Each original quadrant in  
 360 these regions is successively subdivided into four equal-sized children, like quad-trees, until the size  
 361 of refined cells reaches the predefined levels.

362 **4.1 Grid refinement procedure**

363 In this section, we will mainly use a Neumann boundary as an example to illustrate the procedure  
 364 of grid refinement. The rigid boundary is firstly discretized and represented by a set of boundary  
 365 points, and quad-tree cell refinement is carried out point by point sequentially. Initially, each body  
 366 point belongs to a quadrant of the original grid (or cell) system, and we assume that this point is  
 367 always located in the first quadrant of a specific cell, as shown in Fig. 4, in which the cell is drawn  
 in red and the quadrant is plotted as a yellow square with dashed lines.

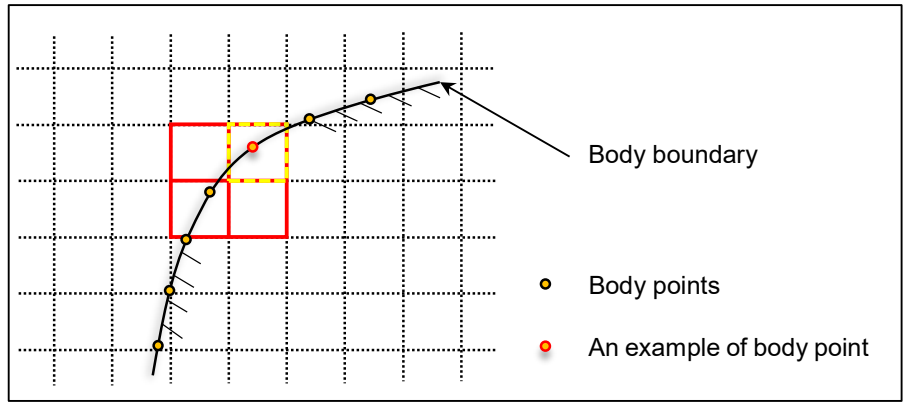


Figure 4: An illustration of one body point located in a cell.

368

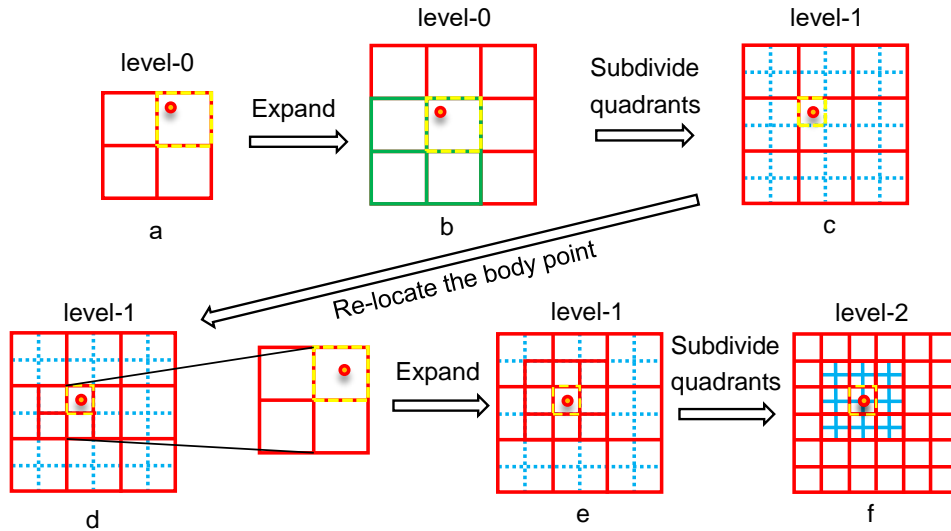


Figure 5: The procedure of level by level subdivision of quadrants for cells containing a body point. Here the maximum quad-tree  $level = 2$  and the  $e-degree = 1$ .

369 We have previously defined cells and quadrants in the original Cartesian grid system. A cell  
 370 owns four quadrants so that the quadrants of overlapping cells simultaneously containing a body  
 371 point shall be equally subdivided. Hereby, the *expansion degree*, for brevity denoted as *e-degree*,

372 is introduced to determine how many cells around this body point shall be taken into account. The  
373 larger the *e-degree* is, the more surrounding cells will be subdivided. In order to distinguish different  
374 levels after a parent quadrant has given birth to four children, the quad-tree *level* is introduced. Note  
375 that the *level* of the original Cartesian grid system is level-0. Fig. 5 shows the steps of subdividing  
376 cells around a body point within *e-degree* = 1. After the subdivision of quadrants of these cells,  
377 the location of the body point in the level-1 small-scale Cartesian grid within the *e-degree* has to  
378 be decided again, as shown in Fig. 5.c-d. The yellow dashed quadrant in the level-1 grid is the next  
379 quadrant which the body point belongs to. This procedure will be successively conducted until it  
380 meets the termination condition. In order to properly capture the body boundary, the grid size of  
381 the deepest-level Cartesian grid system needs to match the size of the boundary elements (defined  
382 as the average distance between adjacent body nodes), i.e.  $\Delta s \approx (\sqrt{2}\Delta x)(1/2)^{level}$ . Here,  $\Delta s$  is the  
383 size of boundary element, and  $\Delta x$  is the horizontal grid size of the original grid system. Since we  
384 use square cells, the vertical grid size  $\Delta z$  is the same as  $\Delta x$ . Therefore, the maximum level of the  
385 quad-tree is determined as

$$level_{\max} = \text{floor} \left[ \frac{\ln(\sqrt{2}\Delta x/\Delta s)}{\ln 2} \right], \quad (26)$$

386 in which the function  $\text{floor}[x]$  outputs the nearest integer less than or equal to  $x$ . Actually, we will  
387 always better refine body elements after determining the maximum level of the grid system to ensure  
388 that there are enough body points in a cell when applying body boundary conditions.

389 After illustrating the quad-tree cell refinement for a single body point above in detail, it is  
390 time to summarize the overall procedure of discretizing the computational domain for a complete  
391 understanding. The basic principle, in brief, is described first point-by-point and then level-by-level:

- 392 1. Locate one of the body points.
  - 393 (a) The associated quadrant and cell are determined.
  - 394 (b) Partition all the targeted quadrants into four equal children.
  - 395 (c) Find the relevant quadrant and cell in the next grid level and divide this into four new
  - 396 children in the next grid level. Repeat steps (a) - (b) until it meets the termination
  - 397 condition.
- 398 2. Repeat step-1 for the next body point until all body points are traversed. Therefore every
- 399 body point is associated with a local cell at the finest level.
- 400 3. Combine all the locally refined expansion regions of all body points into a global grid.

401 In most of the numerical studies presented in this paper, we use *e-degree* = 2 or 3, which is found  
402 sufficient to ensure good accuracy.

## 403 4.2 Quadrant neighbors and node types

404 In the quad-tree grid system, interpolation between different grid levels at the border nodes of  
405 each level is inevitably needed. Therefore, how to identify and interpolate border nodes becomes  
406 important. Normally, a quadrant has at least two and at most four neighbors. In this case, we can  
407 clearly identify border quadrants and interior ones: quadrants with four neighbors are interior while  
408 quadrants with two or three neighbors are on the border of this level. Ma et al. [45] have proven  
409 that the accuracy of interpolation improves when the interpolating point is closer to the cell center.  
410 Therefore, from an accuracy point of view, the solution in border nodes should be interpolated from

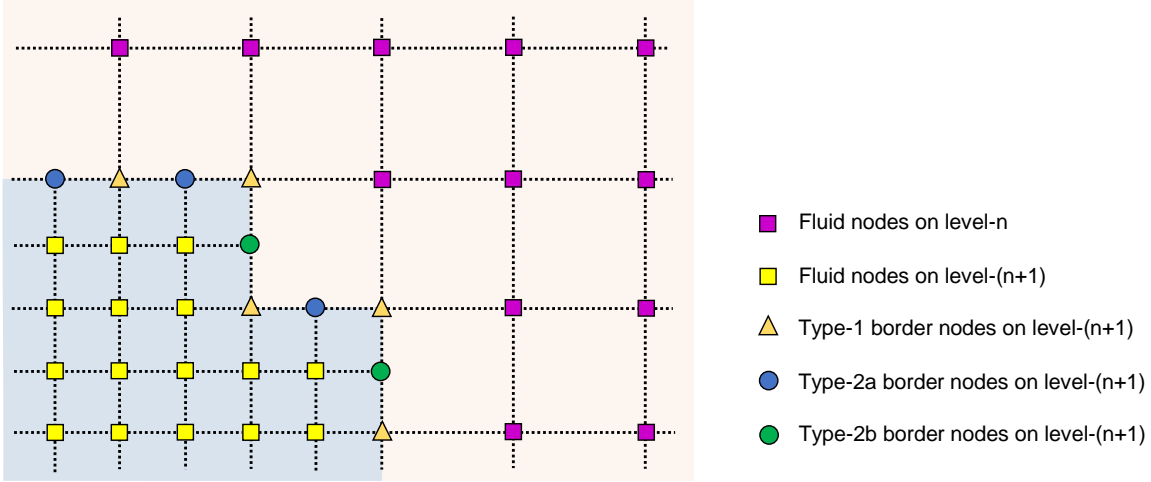


Figure 6: Sketch of a typical quad-tree grid structure with different node types.

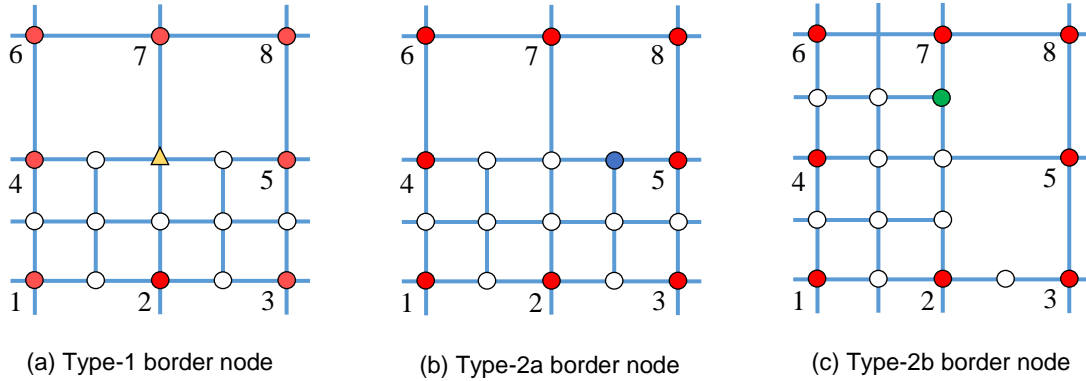


Figure 7: Different types of border nodes using different interpolation strategies.

411 the central area of a cell. Commonly, this cell comes from the parent grid system. Fig. 6 sketches  
 412 a typical quad-tree grid structure of two successive levels. The purple and yellow square nodes are  
 413 typical fluid nodes from the parent and child grid system, respectively, and they naturally locate at  
 414 the center of a cell on their own level.

415 Two types of border nodes between a parent and a child level are also shown in Fig. 7. Type-1  
 416 border nodes belong to cells from the parent grid. The brown triangles lying on the border of the  
 417 refined grid system are Type-1 border nodes. They coincide with nodes in the parent cell and the  
 418 red circular nodes are used for the interpolation while white circles are invalid nodes. Type 2a or  
 419 2b nodes do not coincide with nodes in the parent cell. Note that the red circular nodes in Fig. 7  
 420 are coming from the same parent cell, but in Fig. 7(a) and (b) indices 1~5 are located on child level  
 421 while indices 6~8 are on parent level, and in Fig. 7(c) indices 1, 2, 4, 6, 7 are located on child level  
 422 while indices 3, 5, 8 are on parent level. In these, the solution is interpolated from a parent cell  
 423 where the node is closest to the cell center. Fig. 8 shows an overall distribution of node types on  
 424 different levels, where the node types on the original grids are not displayed.

425 The global algebraic equation systems for both the velocity potential  $\varphi$  and its time derivative

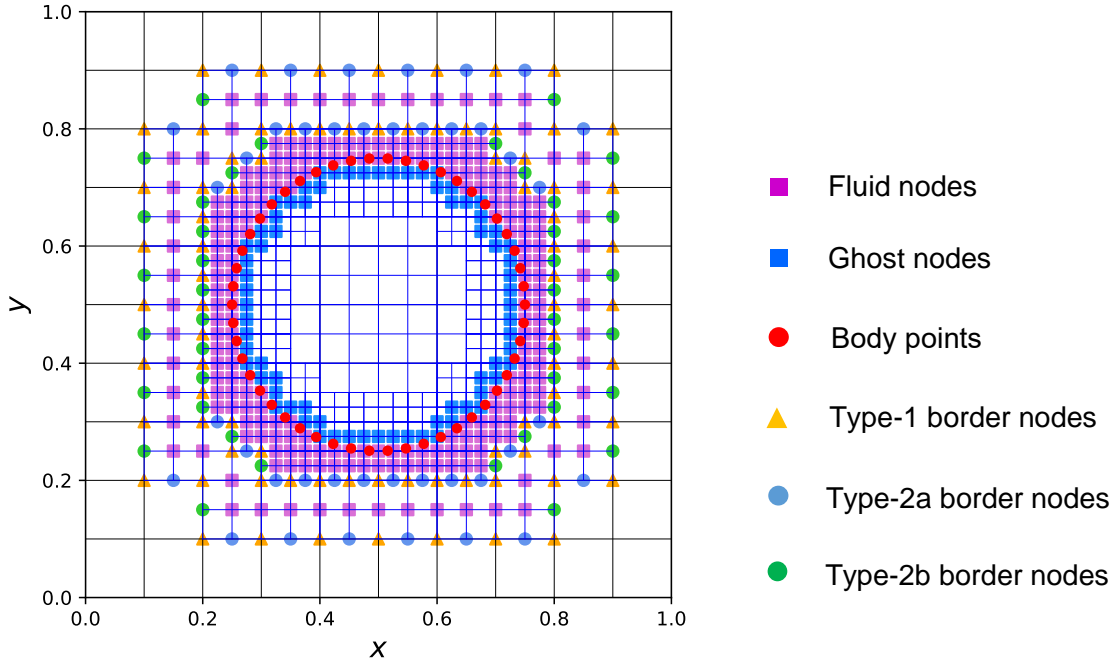


Figure 8: An overall view of an immersed circular cylinder and the associated adaptive cells with different levels and node types. The domain is  $1 \times 1$  and the radius of the ring is 0.25. The  $e$ -degree = 1 and the  $level_{\max} = 2$ .

426  $\varphi_t$  share the same coefficient matrix  $\mathcal{A}$ . Fig. 9 shows an example of the coefficient matrix for a  
 427 fixed circular cylinder in an infinite fluid shown in Fig. 8. The majority of the non-zero entries in  
 428  $\mathcal{A}$  come from the connectivity equations Eq. (13), and are distributed close to the matrix diagonal.  
 429 Those entries are marked by a single integer (either 0, 1 or 2) in the figure. Due to the presence of  
 430 border nodes (Type-1 and Type-2 in Fig. 7) between different levels (marked as  $1 \rightarrow 0$  and  $2 \rightarrow 1$  in  
 431 Fig. 9) and some nodes of the parent cell coming from deeper levels when building the connectivity  
 432 equations (marked as  $0 \rightarrow 1$  and  $1 \rightarrow 2$  in Fig. 9), there are also non-zero entries away from the  
 433 diagonal of the matrix.

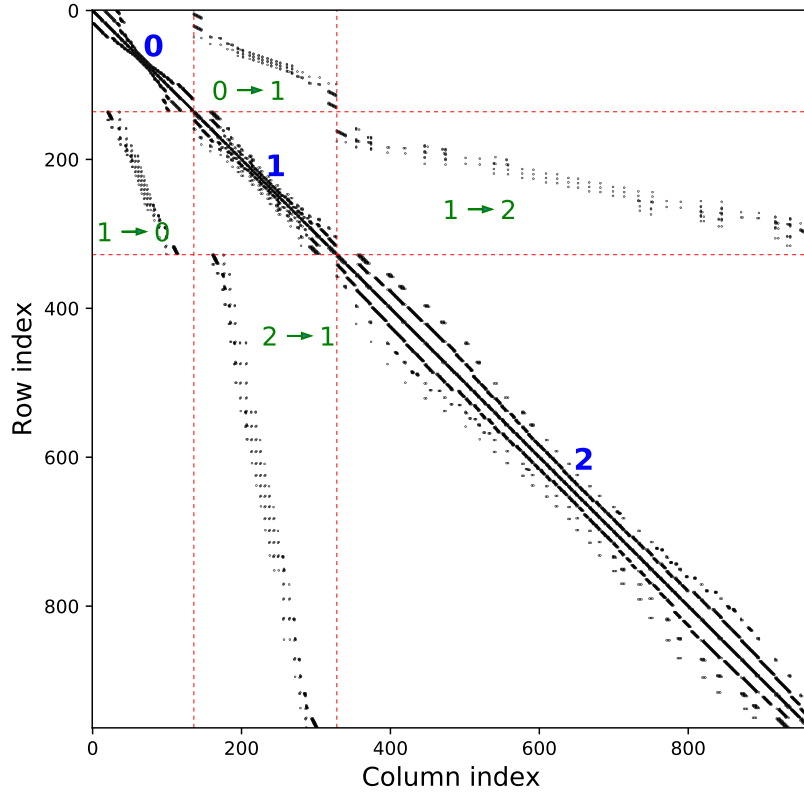


Figure 9: Example of global coefficient matrix in the IB-AHPC method with a rigid circular cylinder in an infinite fluid. Here, the  $e$ -degree = 2 and the  $level_{\max} = 2$ . Level-0, level-1 and level-2 grid are for brevity denoted as 0, 1 and 2, respectively.  $0 \rightarrow 1$  and  $1 \rightarrow 0$  indicate coupling terms between the level-0 and the level-1 grid and vice versa,  $1 \rightarrow 2$  and  $2 \rightarrow 1$  indicate coupling terms between the level-1 and the level-2 grid.

## 434 5 Accuracy and stability of the IB-AHPC

### 435 5.1 Accuracy and spatial convergence analysis

#### 436 5.1.1 A fixed circular cylinder in infinite fluid with a uniform oscillatory flow

437 Here, we consider a fixed submerged circular cylinder with radius  $R$  in an infinite fluid domain  
 438 with a uniform oscillatory flow  $U(t) = U_0 \cos(\omega t)$ . Referring to Fig. 10, a rectangular computational  
 439 domain of  $l_x \times l_y$  is chosen, and the center of the cylinder is coincident with the center of the domain.  
 440 The origin of an Earth-fixed coordinate system,  $Oxy$ , is located at the southwestern corner of the  
 441 computational domain. If potential flow is assumed, an analytical solution for the velocity potential  
 442 is given as [67]:

$$\varphi_{ana}(x, y, t) = U_0 \cos(\omega t) \left( x - \frac{l_x}{2} \right) \left[ 1 + \frac{R^2}{\left( x - \frac{l_x}{2} \right)^2 + \left( y - \frac{l_y}{2} \right)^2} \right]. \quad (27)$$

443 This analytical solution will be used as boundary conditions along Dirichlet boundaries in Fig. 10.  
 444 The Neumann boundary condition  $\partial\varphi/\partial n = \mathbf{U}_{body} \cdot \mathbf{n} = 0$  is applied on the rigid cylinder. The

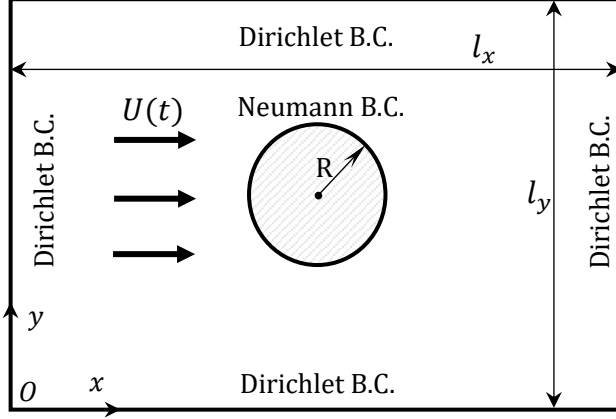


Figure 10: An illustration of a fixed cylinder in the computational fluid domain with a uniform oscillatory flow.

analytical solution of the inline force on the cylinder can be expressed as

$$F_{ana} = -\mu_{ana} \frac{dU}{dt}. \quad (28)$$

Here  $\mu_{ana}$  is an inertia coefficient

$$\mu_{ana} = 2\pi\rho R^2, \quad (29)$$

where  $\rho$  is the fluid density. The  $L_2$ -error is used as a measure of the accuracy of our numerical calculations, which for a general variable  $G$  is expressed as:

$$L_{2,G} = \sqrt{\frac{\sum_{i=1}^N (G_{num,i} - G_{ana,i})^2}{\sum_{i=1}^N G_{ana,i}^2}}. \quad (30)$$

In this case, the grid size in the deepest level,  $dx = \Delta x(1/2)^{level_{max}}$ , is applied, where the original grid size,  $\Delta x/R = 0.42$ , is chosen. In order to match the maximum level, the size of the boundary elements are chosen as the same as the finest grid size, i.e.,  $\Delta s \approx \sqrt{2}\Delta x(1/2)^{level_{max}}$ .

Here, the dimension of the domain is chosen as  $l_x = l_y = 6R$ . Fig. 11 shows the  $L_2$  norm of the error for both the velocity potential on the body points and the inertia constant  $\mu$  with different  $e$ -degree. The four different grid size stands for four levels, i.e. level = 1 ~ 4, of the quad-tree system with the same original grid size. The convergence for the velocity potential on all body nodes, shown on the left-hand side of Fig. 11, is between 3<sup>rd</sup> and 4<sup>th</sup> order versus the non-dimensional grid size on the deepest level, i.e.,  $L_{2,\varphi} \sim (R/dx)^{-3.5}$ . The convergence rate is similar to the original HPC method in [24, 44], indicating that the present IB-AHPC with adaptive cells does not compromise the accuracy of the HPC method. Similarly, the error for the calculated inertia coefficient converges at a rate  $L_{2,\mu} \sim (R/dx)^{-3.5}$ , which agrees well with the accuracy for the velocity potential. We can, moreover, discover that the larger the  $e$ -degree is, the faster the convergence rate will be for the velocity potential, but the improvement is very marginal. The  $e$ -degree also shows negligible influence on the convergence rate for the inertia coefficient, as shown in the right sub-plot in Fig. 11.

Fig. 12 plots the total number of active nodes as a function of  $R/dx$  for different levels of cell refinement and different  $e$ -degree. The total number of grid points for a grid system without local refinement is also included in the figure for comparison. The fitted rate  $k$  indicates that, with local

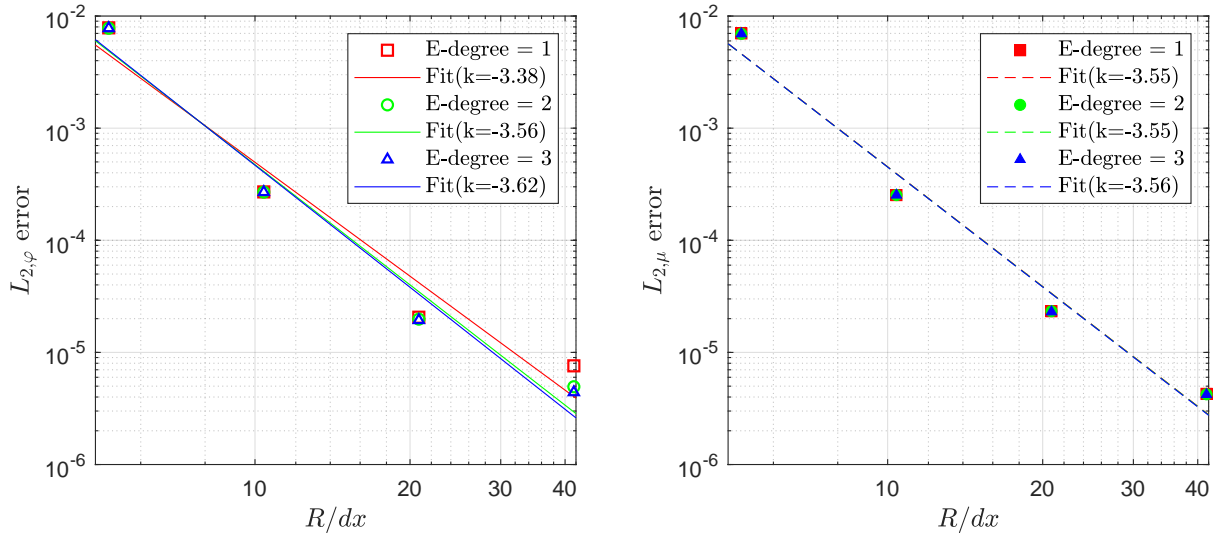


Figure 11: Grid convergence for the solution of a fixed submerged cylinder in a uniform oscillatory flow with different  $e$ -degree. Left: Velocity potential  $\varphi$  on body. Right: Inertia coefficient  $\mu$ . Here,  $dx$  represents the grid spacing in the deepest level grid.

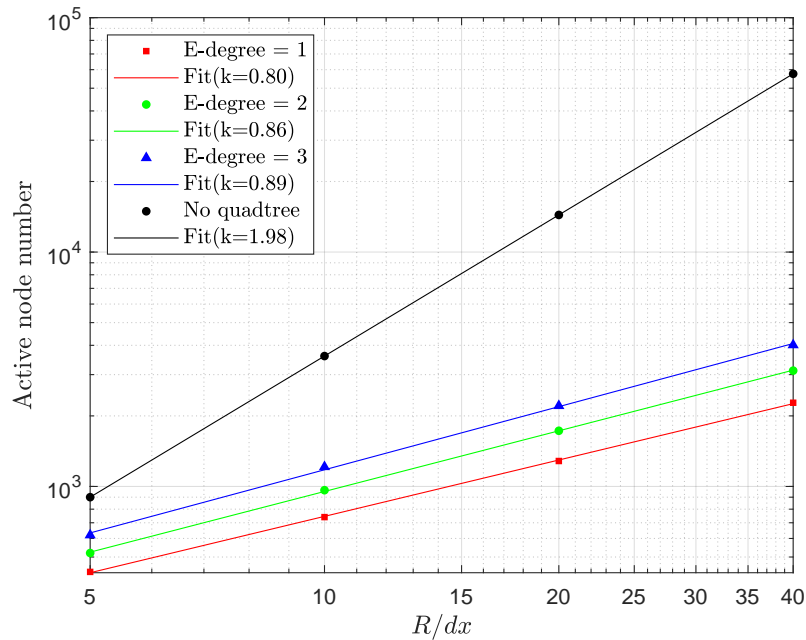


Figure 12: Number of active nodes (unknowns in the global matrix equations) versus grid size for adaptive cells with different  $e$ -degree and cells without quad-tree refinements.

467 cell refinement, the number of unknowns can be dramatically reduced, especially when the local  
 468 grid is significantly refined or for large computational domains. For the considered example, the  
 469 total number of grid points required to reach a given accuracy of solution is found to scale with  
 470  $(1/\Delta x)^{0.8\sim 0.9}$  compared to  $(1/\Delta x)^2$  for a method without local grid refinement. Since the number  
 471 of active nodes is directly associated with the computational cost in solving the global equations, it  
 472 is immediately clear that the cell refinement can greatly save computational cost without sacrificing

473 the accuracy. Generally,  $e\text{-degree} = 2$  or 3 is considered as sufficient, which will also be applied in  
 474 our later simulations to keep a balance between numerical accuracy and computational effort.

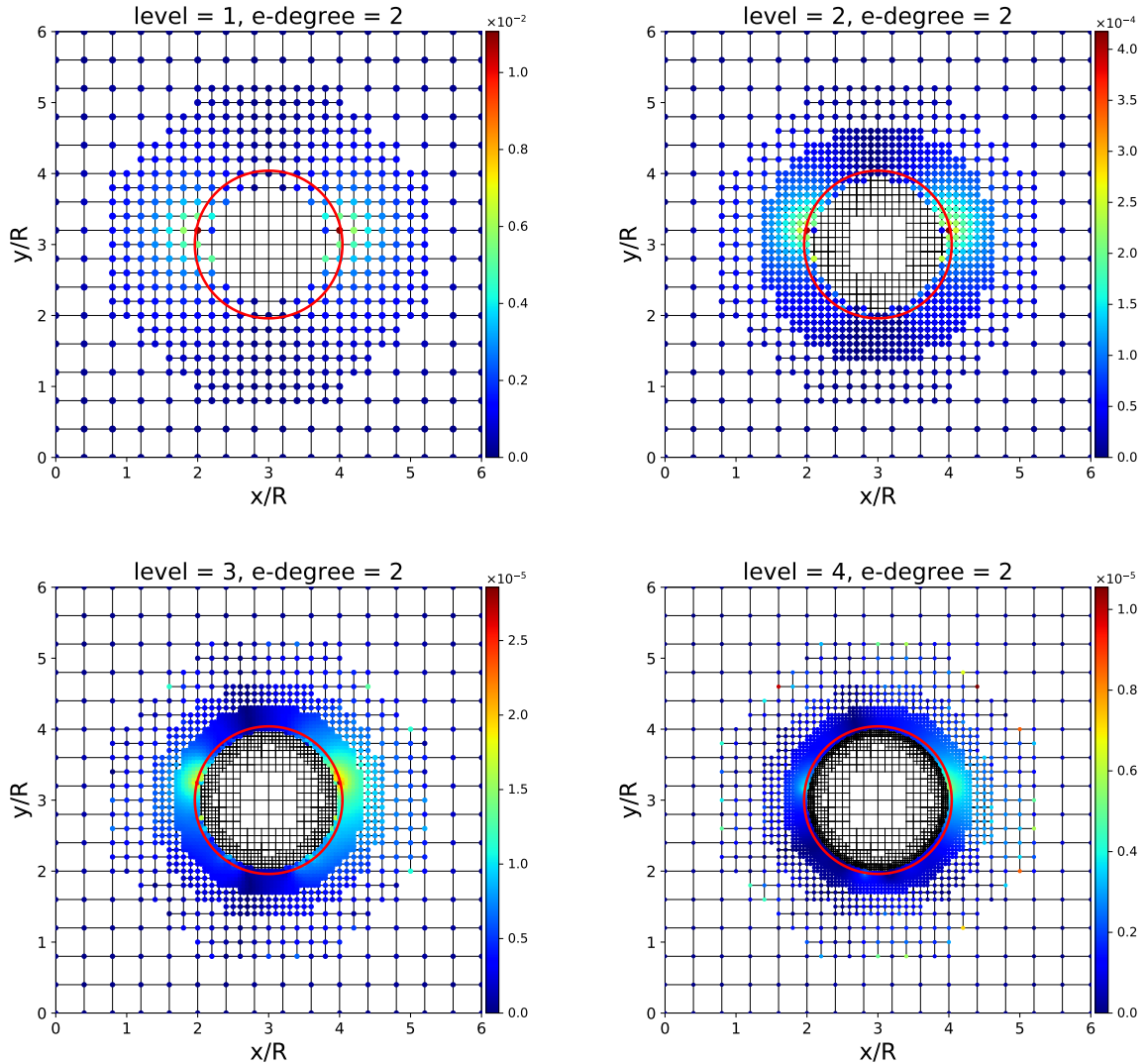


Figure 13: Distribution of  $e_\varphi$  in vicinity of cylinder for different maximum level,  $e\text{-degree} = 2$ .

475 Fig. 13 shows the relative error distribution for the velocity potential in the whole computa-  
 476 tional domain for different levels of quad-tree refinement. The relative error is defined as  $e_\varphi =$   
 477  $|\varphi_{ana} - \varphi_{num}| / \max(|\varphi_{ana}|)$  for each active node, where  $\max(|\varphi_{ana}|)$  is the maximum absolute ana-  
 478 lytical potential in the entire domain. Actually, the error tends to be largest near the body boundary,  
 479 which can be seen from Fig. 13 for level = 1 or 2. But due to the adopting the mode of interpolation  
 480 for Type-2 border nodes in Fig. 7, if given a closer look at these border nodes between level-0 and  
 481 level-1 for the case with level = 4, we can notice that the relative error of some Type-2 nodes tends  
 482 to be larger than that around the body boundary. But this phenomenon disappears between deeper  
 483 levels, namely level-3 and level-4, which might result from the large truncate error in coarse grid.  
 484 On the other hand, the error of Type-1 nodes seems to be smaller than that of two adjacent Type-2  
 485 nodes. This can be explained, from a finite difference point of view, by the fact that the accuracy of  
 486 central difference schemes is better than that for off-centered schemes. In other words, the accuracy  
 487 of interpolation for the HPC method is always the best at the center of a cell.

488 **5.1.2 An oscillating circular cylinder in an infinite fluid**

489 Hanssen et al. [49] in their previous study showed that applying the IBM for a moving structure  
 490 could produce spurious pressure-force oscillations. This issue was solved by Hanssen [47] applying an  
 491 overlapping-grid strategy and solving an extra BVP for the time derivative of the velocity potential,  
 492 however, with a cost of increased complexity of numerical implementation and somewhat larger  
 493 computational effort. In this section, we show that the spurious force oscillations can be eliminated  
 494 by using the Lagrangian acceleration potential method (LAPM) described in Section. 3.3 when  
 495 applying the IBM to a moving structure.

496 To demonstrate this, we consider the forced harmonic oscillation of the circular cylinder in an  
 497 infinite fluid, which has also been studied by Hanssen et al. [49]. The cylinder is initially set in the  
 498 center of the computational domain with  $l_x = l_y = 20R$ . The motion of the center of the cylinder in  
 499 surge is given as:

$$\begin{cases} x_c(t) = \frac{l_x}{2} + \frac{U_c}{\omega} \sin \omega t, \\ y_c(t) = \frac{l_y}{2}. \end{cases} \quad (31)$$

500 Here  $U_c$  is velocity amplitude,  $\omega$  is the oscillatory frequency. The motion amplitude is set to be  
 501  $U_c/\omega = 4R$ . The analytical solution for the velocity potential in this case is

$$\varphi_{ana}(x, y, t) = -U_c \cos(\omega t) \cdot (x - x_c(t)) \left[ \frac{R^2}{(x - x_c(t))^2 + (y - y_c(t))^2} \right]. \quad (32)$$

502 The analytical linear hydrodynamic force on body surface due to the harmonic oscillation is

$$f_x(t) = -\rho \oint_{\Gamma_S} \frac{\partial \varphi}{\partial t} n_x ds = f_0 \sin(\omega t) \quad (33)$$

503 where  $f_0 = \rho\pi\omega R^2 U_c$ ,  $\rho$  is the fluid density and  $n_x$  is the horizontal component of the normal vector  
 504 on the surface  $\mathbf{n} = (n_x, n_y)$ , defined as positive pointing into the body.

505 The grid spacing in this case is the same as that for the fixed cylinder case.  $level_{\max}$  ranging  
 506 from 1 to 4 is applied to study the convergence of  $f_x$ . The time step  $\Delta t = T/252 = 0.05s$ , and three  
 507 different velocity amplitudes are considered:  $U_c = 1.0m/s, 2.0m/s$  and  $2.5m/s$ . Here  $T = 2\pi/\omega$ .  
 508 Analytical Dirichlet boundary conditions are applied along the four boundaries of the computational  
 509 domain. Fig. 14 shows the  $L_2$  error of  $f_x$  with three different velocity amplitudes as well as the  
 510 error of the inertia coefficient for a fixed cylinder for comparison. It is expected that the oscillating  
 511 velocity amplitude has almost no impact on the convergence rate. Although the error for fixed cases  
 512 is smaller than that for oscillating cases, the convergence rates of  $f_x$ ,  $L_{2,f_x} \sim (R/dx)^{-3.0 \sim -4.0}$ , for  
 513 the oscillation cases are in the same range as that for a fixed cylinder, which is different from the  
 514 observation in [49].

515 Hanssen et al. [49] and Kontos [56] have computed the acceleration potential  $\varphi_t$  using the finite  
 516 difference method (FDM), and obtained highly oscillatory force signals. These spurious oscillations  
 517 can be reduced by increasing the time step size and by decreasing grid spacing. Here, we also compute  
 518 the acceleration potential by applying the the EAPM and the LAPM, as described in § 3.3. In both  
 519 cases, the moving velocity amplitude  $U_c = 1.0m/s$ . We also set two time steps  $\Delta t = T/1260 = 0.01s$   
 520 and  $\Delta t = T/252 = 0.05s$ . As shown in Fig. 15 (left column) for the LAPM, the time series of force on  
 521 the harmonically oscillating cylinder agree very well with the analytical solution from Eq. (33). We  
 522 also include in this plot the results obtained by using the EAPM (middle column) and a simple first-  
 523 order backward FDM (right column). The results demonstrate that the LAPM is a very promising  
 524 approach in eliminating the force oscillations, and its robustness is independent of the time step size,

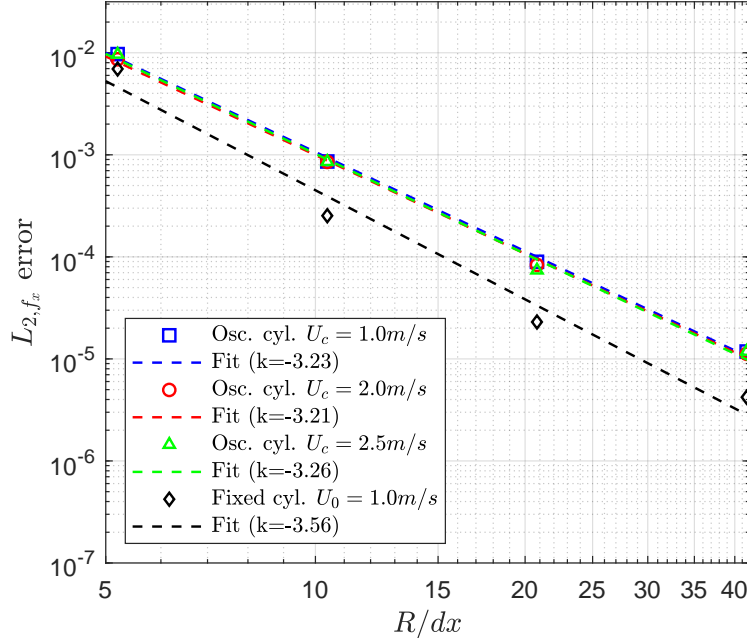


Figure 14: Grid convergence of  $f_x$  on an oscillating submerged cylinder with three different amplitudes of velocity in undisturbed fluid. The error of the inertia coefficient  $L_{2,\mu}$  for a fixed cylinder is also demonstrated for comparison. Here,  $dx$  represents the grid spacing in the deepest level grid.

525 in contrast to the EAPM and the FDM. Increasing local refinement from  $level_{\max} = 1$  to 3 is also  
 526 seen to reduce the oscillations for both the EAPM and the FDM results, especially for larger time  
 527 steps, but somehow we can tell that the 1<sup>st</sup>-order FDM seems to perform slightly better than the  
 528 EAPM in this case.

529 Fig. 16 compares the CPU time per time step of generating global matrix system and solving  
 530 global equations for  $\varphi$  and  $\varphi_t$  by using the FDM, the EAPM and the LAPM. In the plot, we also  
 531 displayed the CPU time per time step by using different grid size, i.e. different grid  $level_{\max}$ . In  
 532 practice, the BVPs for the velocity potential  $\varphi$  and acceleration potential  $\varphi_t$  share the same global  
 533 coefficient matrix, then extra time needs to be spent on the generation of the right-hand-side vector  
 534 for  $\varphi_t$ , and on solving the equations. We can find that the time spent for the EAPM and the LAPM  
 535 is almost the same even if it is slightly higher for the EAPM, and the time is nearly twice more than  
 536 that of the FDM.

## 537 5.2 Stability analysis

538 To assess the stability of the present IB-AHPC method, a matrix-based stability study is con-  
 539 ducted in this section. Here, we consider a linear numerical wave tank without any structures in the  
 540 fluid or at the free surface. We consider the linearized kinematic and dynamic free-surface conditions  
 541 in matrix form in 2D:

$$\frac{\partial}{\partial t} \begin{bmatrix} \eta \\ \tilde{\varphi} \end{bmatrix} = \begin{bmatrix} 0 & \frac{\partial}{\partial z} \\ -g & 0 \end{bmatrix} \begin{bmatrix} \eta \\ \tilde{\varphi} \end{bmatrix}, \quad (34)$$

542 where  $\eta$  is the surface elevation and  $\tilde{\varphi} = \varphi(x, 0, t)$  is the velocity potential at the free surface. The  
 543 free surface will be discretized into a set of wave markers, as described in § 3.2. As a result, a

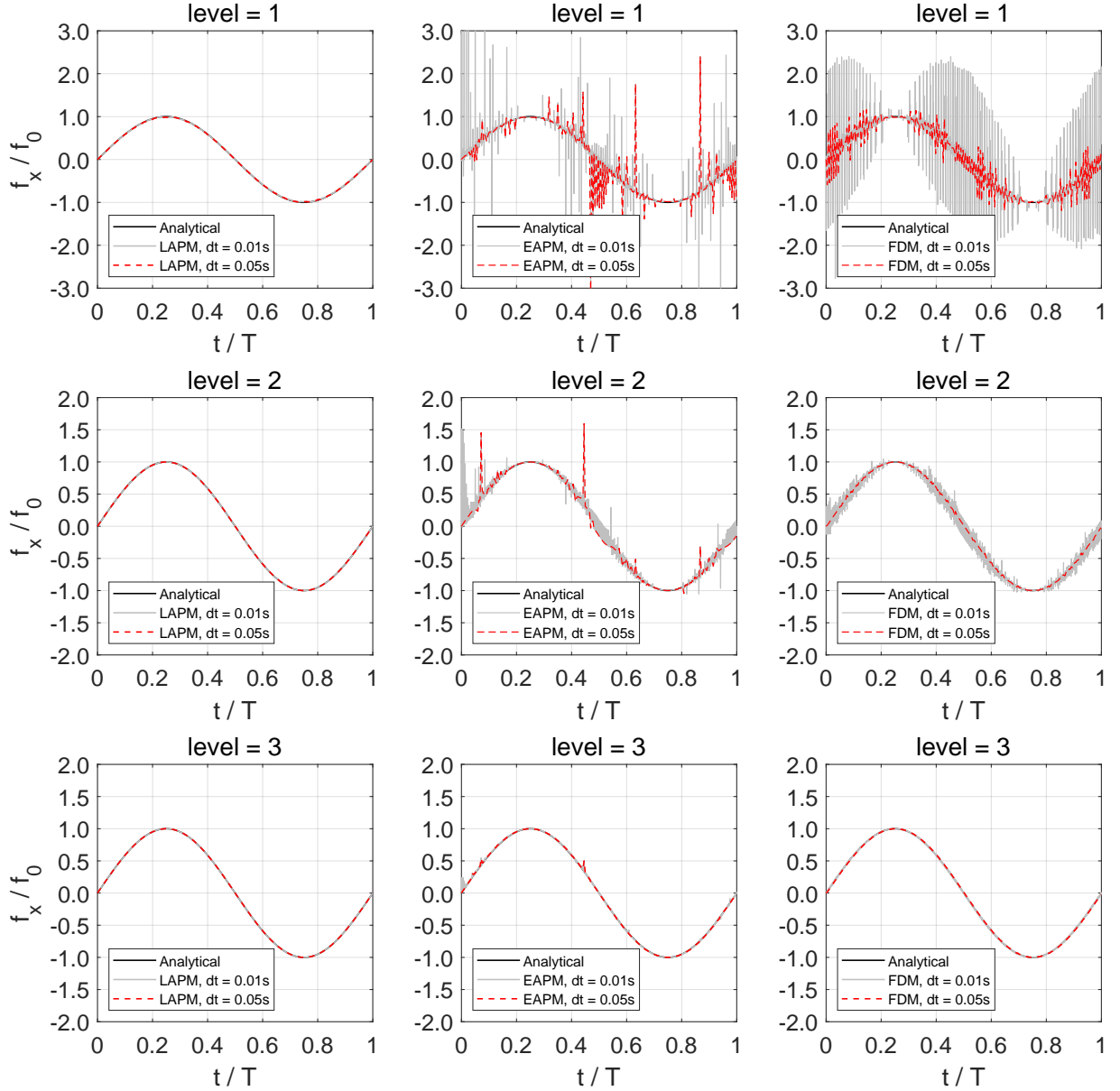


Figure 15: Time series of force  $f_x$  on an oscillating cylinder in infinite still fluid using the LAPM (left), the EAPM (middle) and the FDM (right) for different  $level_{\max}$ , respectively.

544 space-discretized form of Eq. (34) can be rewritten as

$$\frac{\partial}{\partial t} \begin{bmatrix} \boldsymbol{\eta} \\ \tilde{\boldsymbol{\varphi}} \end{bmatrix} = \begin{bmatrix} 0 & \mathcal{L} \\ -g\mathcal{I} & 0 \end{bmatrix} \begin{bmatrix} \boldsymbol{\eta} \\ \tilde{\boldsymbol{\varphi}} \end{bmatrix} \Rightarrow \frac{\partial \mathbf{f}}{\partial t} = \mathcal{J}\mathbf{f}. \quad (35)$$

545 Here  $\mathbf{f} = [\eta_1, \eta_2, \dots, \eta_{N_m}, \tilde{\varphi}_1, \tilde{\varphi}_2, \dots, \tilde{\varphi}_{N_m}]^T$  vector is the combination of the free-surface elevation and  
 546 velocity potential at all wave markers. The identity matrix  $\mathcal{I}$  and the operator matrix  $\mathcal{L}$  are  $N_m \times N_m$ ,  
 547 where  $N_m$  is the number of wave markers.  $\mathcal{J}$  denotes the Jacobian matrix. In the global linear  
 548 equations system  $\mathcal{A}\boldsymbol{\varphi} = \mathbf{e}$  with  $N$  unknowns,  $\tilde{\boldsymbol{\varphi}}$  can be distributed in the corresponding positions in  
 549 the right-hand side vector  $\mathbf{e}$  in the form of

$$\mathcal{Q}_{N \times N_m} \tilde{\boldsymbol{\varphi}}_{N_m \times 1} \simeq \mathbf{e}_{N \times 1}, \quad (36)$$

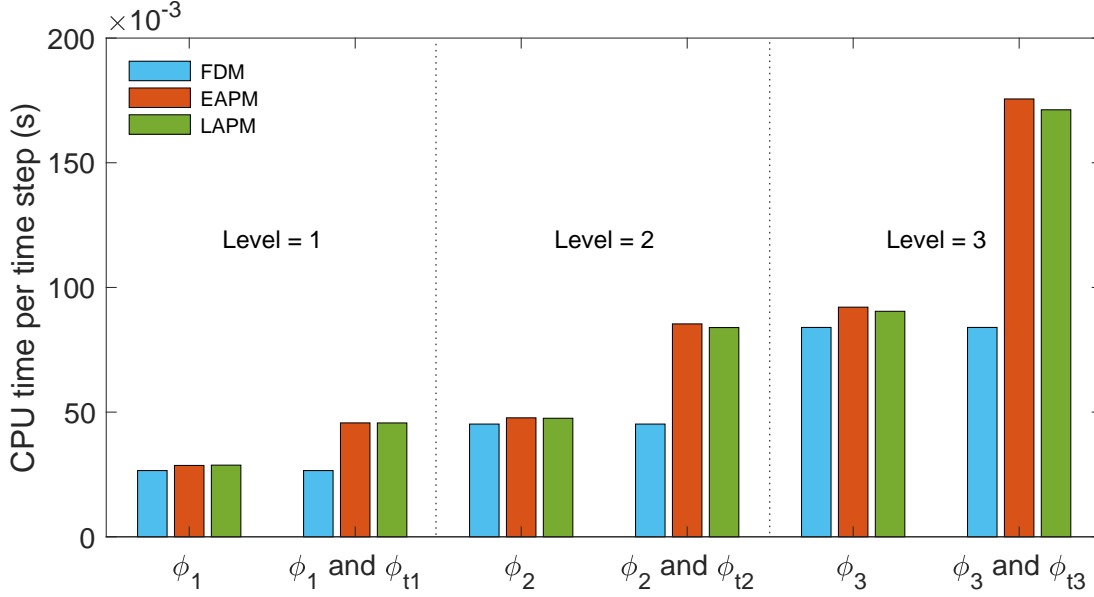


Figure 16: CPU time per time step of generating global matrix system and solving equations for  $\varphi$  (left), and total CPU time per time step of generating global matrix system and solving equations for  $\varphi$  and  $\varphi_t$  (right) by using the FDM, the EAPM and the LAPM. The subscript number in this figure denotes different  $level_{\max}$  and  $\varphi_t$  represents either Eulerian or Lagrangian acceleration potential.

550 by an operator matrix  $\mathcal{Q}$ . Note that the left-hand side and the right-hand side of Eq. (36) are not  
 551 exactly the same, with a constant term missing, which however is independent of  $\tilde{\varphi}_{N_m \times 1}$ . Neglecting  
 552 this constant term will not influence the results of the stability analysis. Hence, we can also get the  
 553 following relations:

$$\mathcal{A}_{N \times N}^{-1} \mathcal{Q}_{N \times N_m} \tilde{\varphi}_{N_m \times 1} \simeq \varphi_{N \times 1}. \quad (37)$$

554 After taking the vertical derivatives of the velocity potential  $\varphi_{N \times 1}$  by an operator matrix  $\mathcal{D}$ :

$$(\mathcal{D}_{N_m \times N} \mathcal{A}_{N \times N}^{-1} \mathcal{Q}_{N \times N_m}) \tilde{\varphi}_{N_m \times 1} \simeq \mathcal{D}_{N_m \times N} \varphi_{N \times 1}, \quad (38)$$

555 we finally obtain the operator matrix  $\mathcal{L}$  in the form of

$$\mathcal{L} = \mathcal{D} \mathcal{A}^{-1} \mathcal{Q}. \quad (39)$$

556 For a given discrete system, we can compute the operator matrix  $\mathcal{L}$  and hence complete the Jaco-  
 557 bian matrix  $\mathcal{J}$  in Eq. (35). For the discretization of the free-surface boundary conditions discussed  
 558 above, the eigenvalues of the matrix  $\mathcal{J}$  are purely imaginary and can be calculated numerically. To  
 559 guarantee stability, the maximum eigenvalue of matrix  $\mathcal{J}$  multiplied by the time step  $\Delta t$  must be  
 560 inside the stability region for a given time stepping scheme. For the 4<sup>th</sup>-order explicit Runge-Kutta  
 561 (RK4) scheme used in our study, the stability contour can be expressed as

$$\beta(\lambda \Delta t) = 1 + \lambda \Delta t + \frac{(\lambda \Delta t)^2}{2!} + \frac{(\lambda \Delta t)^3}{3!} + \frac{(\lambda \Delta t)^4}{4!}, \quad (40)$$

562 where  $\lambda$  is an eigenvalue of matrix  $\mathcal{J}$ . For a stable solution, we need to have

$$|\beta(\lambda \Delta t)| \leq 1. \quad (41)$$

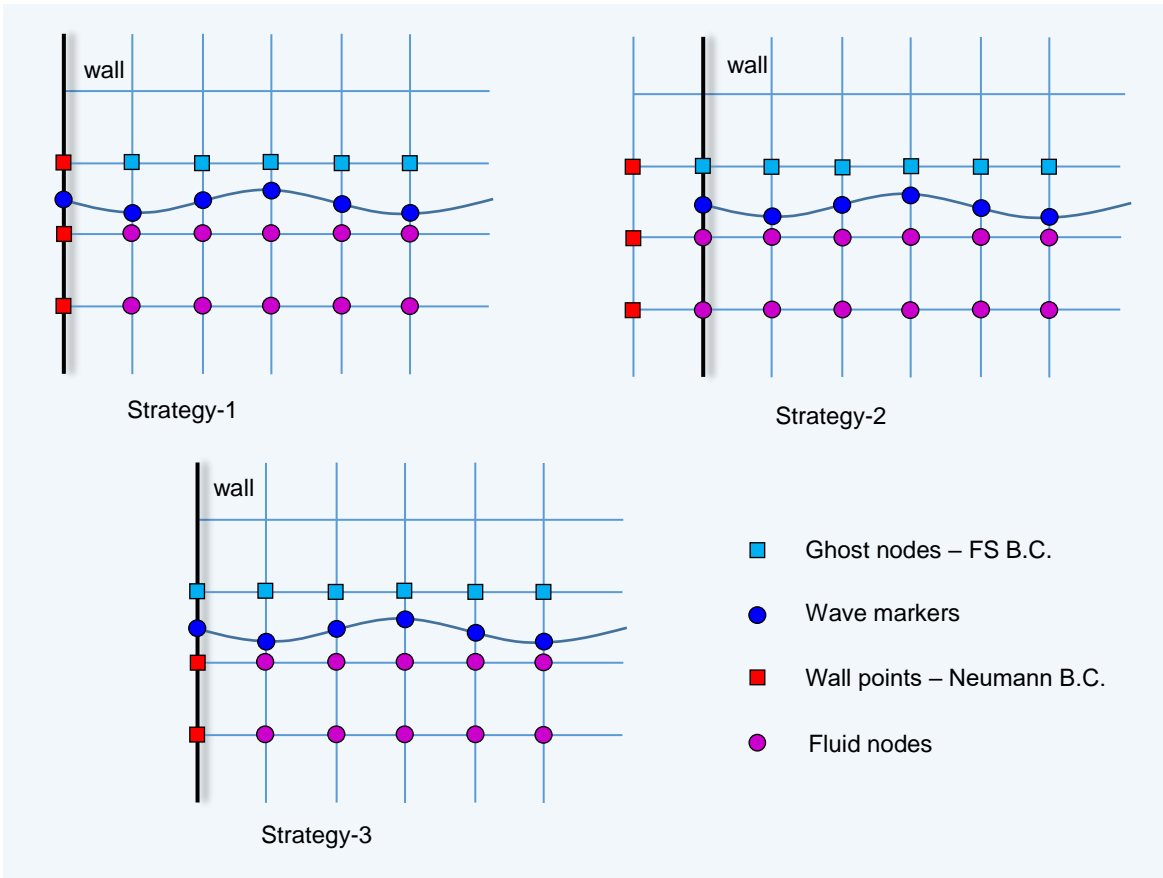


Figure 17: Three strategies to deal with markers on walls.

563 Since the eigenvalues of  $\mathcal{J}$  are purely imaginary, the contour of Eq. (40) intersects with the imaginary  
 564 axis at  $\pm 2\sqrt{2}j$ , where  $j = \sqrt{-1}$ , i.e.  $|\lambda_{\max}|\Delta t \leq 2\sqrt{2}$ .

565 Up to this point, the influence of grid spacing, time stepping and choice of boundary conditions on  
 566 the stability can be explored by this stability analysis procedure. In general, the instability problem  
 567 always tends to happen at the free surface, particularly at the intersection of the wave profile and a  
 568 Neumann boundary. To deal with the wave marker along the left wall boundary, Strategy-3 in Fig. 17  
 569 was first adopted where the ghost node above this wave marker is regarded as a Dirichlet boundary  
 570 node using the free surface boundary conditions. However, instability occurs when this strategy is  
 571 applied, even for generating waves with very small wave slope and amplitude. This kind of instability  
 572 always starts with markers on the left and right walls oscillating irregularly and eventually leads to  
 573 the breakdown of the computation. In order to increase the stability of the whole system, two other  
 574 strategies are put forward, i.e. Strategy-1 and Strategy-2 in Fig. 17. For Strategy-1, the ghost node  
 575 above the wave marker on the wall will be regarded as a Neumann boundary node, but shares the  
 576 coordinates of this wave marker when producing the global linear equation system. This kind of  
 577 strategy is very easy to implement. In Strategy-2, the ghost node with respect to the wave marker  
 578 on the wall is treated as in Strategy-3, while the original wall nodes are regarded as fluid nodes and  
 579 a set of ghost nodes is added outside of the wall sharing information from the corresponding nodes  
 580 on the wall. The difference between Strategy-2 and Strategy-3 is that the wave marker in Strategy-2  
 581 is located at the middle vertical line of a cell but in Strategy-3, it lies on the left border line of a  
 582 cell. This feature of Strategy-2 can increase the stability of the numerical model and can also be

583 beneficial to accuracy.

Table 2: Maximum eigenvalues  $\lambda_{\max}$  of three strategies for different maximum level of quadtree and  $e$ -degree.

|            |   | $level_{\max}$            |                           |                           |                           |
|------------|---|---------------------------|---------------------------|---------------------------|---------------------------|
|            |   | 1                         | 2                         | 3                         | 4                         |
| Strategy-1 | 1 |                           |                           |                           |                           |
|            | 2 | $0 \pm 11.66j$            | $0 \pm 16.49j$            | $0 \pm 23.32j$            | $0 \pm 32.98j$            |
|            | 3 |                           |                           |                           |                           |
| Strategy-2 | 1 |                           |                           |                           |                           |
|            | 2 | $0 \pm 11.66j$            | $0 \pm 16.49j$            | $0 \pm 23.32j$            | $0 \pm 32.98j$            |
|            | 3 |                           |                           |                           |                           |
| Strategy-3 | 1 | $0 \pm 11.66j$            | $0 \pm 16.49j$            | $0 \pm 23.32j$            | $0 \pm 1.65 \times 10^9j$ |
|            | 2 | $0 \pm 2.20 \times 10^8j$ | $0 \pm 2.25 \times 10^8j$ | $0 \pm 2.37 \times 10^8j$ | $0 \pm 2.42 \times 10^8j$ |
|            | 3 | $0 \pm 1.95 \times 10^8j$ | $0 \pm 2.24 \times 10^8j$ | $0 \pm 2.14 \times 10^8j$ | $0 \pm 2.91 \times 10^8j$ |

584 Table 2 gives the maximum eigenvalues from the matrix-based stability analysis for these three  
585 strategies of handling wave markers on walls with different  $e$ -degree and depth of grid level. From this  
586 table, an unexpected observation is that Strategy-1 and Strategy-2 share the same eigenvalues with  
587 the same grid refinements; here, it is very clear and reasonable that the  $e$ -degree plays a minor role  
588 in influencing the stability. On the other hand, we can see that most of the eigenvalues for Strategy-  
589 3 are many orders of magnitude larger than that for the other strategies. This stability analysis  
590 of Strategy-3 provides a mathematical perspective to explain the instability occurring during the  
591 computation. Although the eigenvalues for Strategy-3 at  $e$ -degree = 1,  $level_{\max} = 1 \sim 3$  are the  
592 same as Strategy-1 and Strategy-2, we have to mention that the calculation of the linear waves fails  
593 to match perfectly with the analytical solution while the other two strategies give good results.

594 Since Strategy-1 and Strategy-2 share the same maximum eigenvalues, we can assume that they  
595 will exhibit the same stability behavior. Fig. 18 shows the eigenvalues of the Strategy-1 distributed  
596 within the stable region of the RK4 scheme for different  $level_{\max}$  of the quad-tree. All eigenvalues  
597 in this linear stability analysis are on the imaginary axis, and the horizontal distance between the  
598 numerical stability eigenvalue and the stability contour of the RK4 scheme indicates how much  
599 numerical diffusion is introduced. In this case, although this strategy is stable for all grid refinements,  
600 it can be predicted that the numerical diffusion introduced is the least with the finest grid and the  
601 most with the coarsest grid, since not all eigenvalues are on the RK4 contour when level = 1.

602 As discussed by Engsig-Karup et al. [33], the continuous eigenvalue of the Jacobian matrix  $\mathcal{J}$  in  
603 Eq. (35) is simply the wave circular frequency  $\sqrt{gk \tanh(kh)}$ , where  $g$  is the gravitational acceleration,  
604  $k$  is the wave number and  $h$  is mean water depth. Therefore, we plot the maximum eigenvalues  
605 normalized by the Nyquist circular frequency  $\omega_N = \sqrt{gk_N \tanh(k_N h)}$ , versus the normalized grid  
606 size  $L_w/\Delta x$  ( $L_w$  is wave length) for Strategy-1 and -2 in Fig. (19)(a). Here the four dotted red circles  
607 correspond to the four different  $level_{\max}$  of the grid system. The Nyquist wave number is defined  
608 as  $k_N = \pi/\Delta x$ . Noticeable is that the normalized maximum eigenvalues are independent of the grid  
609 spacing in our numerical model since we use square cells. In other words, it implies that the stability  
610 of the system is not sensitive to how many levels of grids are used as long as  $\Delta x = \Delta z$ .

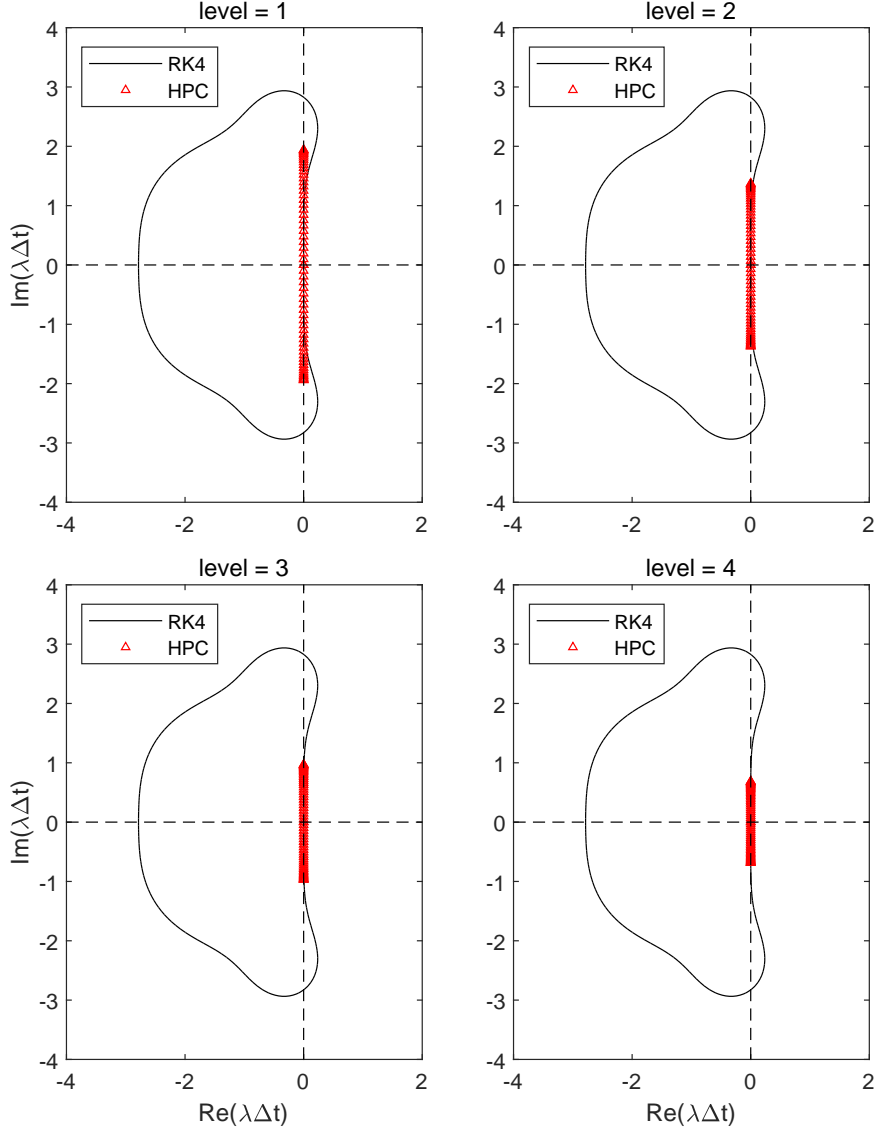


Figure 18: Distribution of  $\lambda\Delta t$  within the stability region of the explicit RK4 scheme for Strategy-1 with different quad-tree levels.

611 Fig. 19(b) shows the tendency of the maximum eigenvalues  $\lambda_{\max}/\omega_N$  versus mesh aspect ratio  
612  $\Delta z/\Delta x$ . The number of stencils along the wave tank length and height is fixed at  $N_x = 20$  and  
613  $N_z = 10$ . As the cells are highly horizontally stretched ( $\Delta z/\Delta x \ll 1$ ) or highly vertically stretched  
614 ( $\Delta z/\Delta x \gg 1$ ), the maximum eigenvalue increases in an exponential tendency both for Strategy-1  
615 and -2. The tendency ratio is of  $(\Delta z/\Delta x)^{-1.0}$  for vertically stretched cells and of  $(\Delta z/\Delta x)^{0.5}$  for  
616 horizontally stretched cells, which means the system imposes a much more severe stability require-  
617 ment in these conditions. On the other hand, there is an asymptotic limit  $\lambda/\omega_N = 0.857$  when the  
618 mesh aspect ratio  $\Delta z/\Delta x = 1$ . This observation tells us that square cells used in numerical mod-  
619 els can guarantee the stability regardless of the grid refinement, and make the computation more  
620 stable than stretched cells. In addition, square cells also introduce the minimum error compared  
621 to distorted or stretched cells according to the study by Ma et al. [45]. These investigations and  
622 observations provide a strong motivation for using cells with mesh aspect ratio  $\Delta z/\Delta x = 1$ . Another

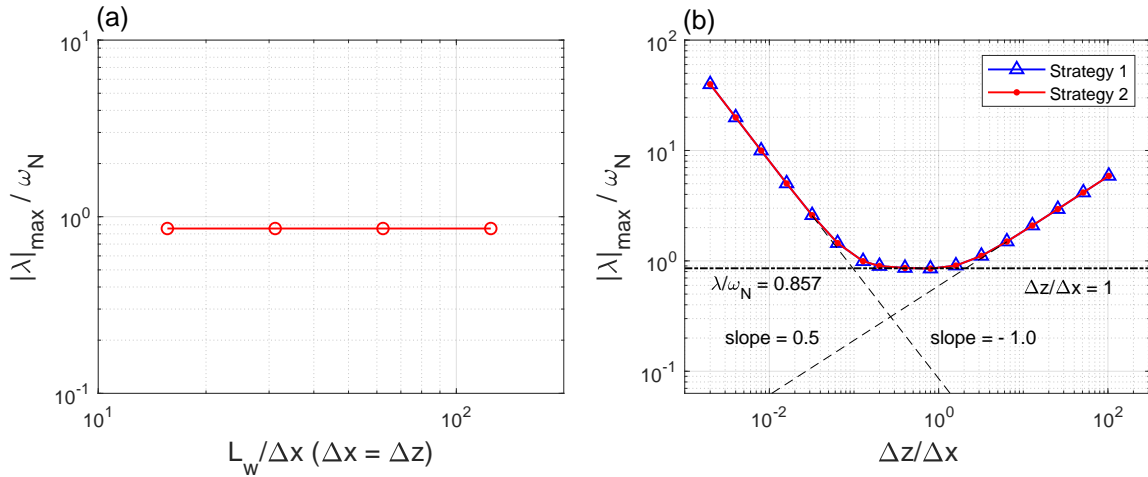


Figure 19: (a) Maximum eigenvalues vs. grid size; (b) Maximum eigenvalues vs. mesh aspect ratio for Strategy-1 and Strategy-2.

623 point is that Strategy-1 and Strategy-2 share the same stability performance. Considering the much  
 624 easier implementation of Strategy-1, this strategy will be used in the following wave-body interaction  
 625 study.

## 626 6 Numerical applications

### 627 6.1 Generation of periodic waves in a nonlinear wave tank

628 In this section, generation of periodic waves in a fully-nonlinear numerical wave tank with finite  
 629 water depth is considered. Fig. 20 shows a sketch of the numerical wave tank, where we in the  
 630 present study use a wave-making zone  $L_{W_{MZ}} = L_w$  and wave-absorbing zone  $L_{W_{DZ}} = 2.3L_w$ , where  
 631  $L_w = 2.6m$  is the wave length.  $\partial\Omega_{left}$ ,  $\partial\Omega_{right}$  and  $\partial\Omega_{seabed}$  are Neumann boundaries. The length of  
 632 this wave tank is  $L = 20m$  and the water depth is  $h = 2.5m$ . A global Cartesian coordinate system  
 633  $Oxz$  is located on the mean water line at the middle of this tank with  $z$ -axis pointing upwards.  
 634 The free surface is represented by a set of wave markers, which are only allowed to move vertically.  
 635 Namely, the semi-Lagrangian free surface tracking is applied. More details on the semi-Lagrangian  
 636 method of dealing with the free-surface dynamic and kinematic free-surface conditions can be found  
 637 in, e.g. [51] and [47]. The number of wave markers is equal to the number of grid points along the  
 638  $x$ -axis in the deepest level.

639 The velocity potential and elevation of the free surface from the high-order solution of stream  
 640 function by [68] or [69] are given as input signals at each time step. One could also refer to an  
 641 algorithm of high efficiency and arbitrary precision provided by Clamond and Dutykh [70]. A zero-  
 642 penetration Neumann boundary condition  $\partial\varphi/\partial n = 0$  is imposed on  $\partial\Omega_{left}$ ,  $\partial\Omega_{right}$  and  $\partial\Omega_{seabed}$ .  
 643 The first 20 Fourier components are included in this study.

644 In the wave-making zone, a relaxation is performed after each time-integration of the kinematic  
 645 and dynamic free-surface boundary conditions by using the 4<sup>th</sup>-order explicit Runge-Kutta (RK4)  
 646 scheme. The relaxation method is one of the most widely employed techniques for wave generation  
 647 or absorption since it is very flexible and straightforward to implement [3, 71, 72, 73, 74]. After  
 648 relaxation, the free-surface elevation and velocity potential on the free surface are given as:

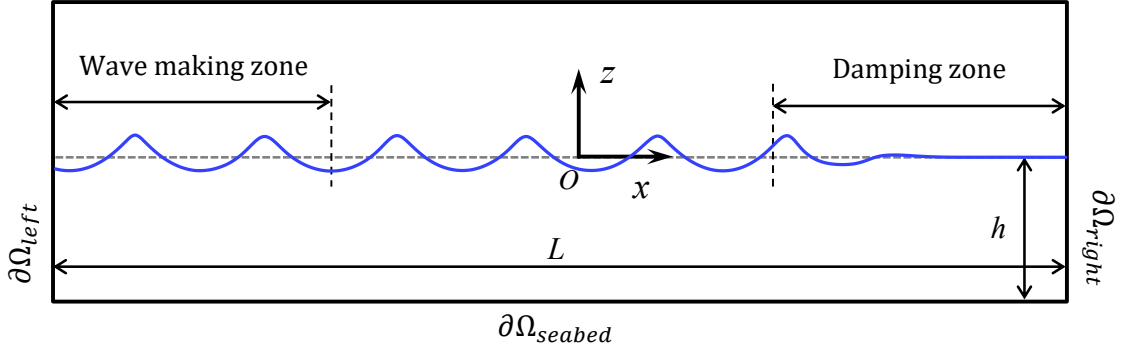


Figure 20: Sketch of a numerical wave tank.

Table 3: Definition of periodic waves.

|        | $ka$ | $H(m)$ | $T(s)$ | $k(m^{-1})$ | $level_{\max}$ | $CFL$       |
|--------|------|--------|--------|-------------|----------------|-------------|
| Case-1 | 0.1  | 0.0828 | 1.284  | 2.417       | 1 2 3          | 0.5         |
| Case-2 | 0.2  | 0.1660 | 1.265  | 2.417       | 2              | 0.3 0.6 0.9 |
| Case-3 | 0.3  | 0.2480 | 1.234  | 2.417       | 1 2 3          | 0.5         |
| Case-4 | 0.4  | 0.3310 | 1.192  | 2.417       | 2              | 0.3 0.6 0.9 |

$$\begin{aligned}\eta_{new}(x, t) &= \gamma_r(x)\eta_{ref}(x, t) + [1 - \gamma_r(x)]\eta_{num}(x, t), \\ \varphi_{m,new}(x, t) &= \gamma_r(x)\varphi_{m,ref}(x, t) + [1 - \gamma_r(x)]\varphi_{m,num}(x, t),\end{aligned}\quad (42)$$

649 where,  $\eta_{num}$  and  $\eta_{ref}$  are the numerical result from time-integration and the reference solution,  
650 respectively, while  $\varphi_{m,num}$  and  $\varphi_{m,ref}$  represent the numerical and the reference velocity potentials.  
651 One of the most prevalent relaxation functions  $\gamma_r(x)$  is proposed by Fuhrman et al. [72] as

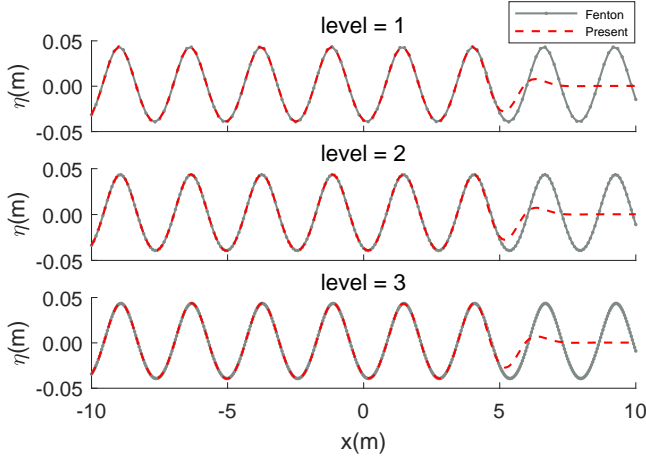
$$\gamma_r(x) = \begin{cases} \frac{\exp((1 - x_r)^{3.5}) - 1}{\exp(1) - 1}, & x - x_0 \leq L_{WMZ} \\ 0, & x - x_0 > L_{WMZ} \end{cases}\quad (43)$$

652 where  $x_r = (x - x_0)/L_{WMZ}$  is the local coordinate within the wave making zone.  $x_0$  corresponds to  
653 the position of  $\Omega_{left}$ .

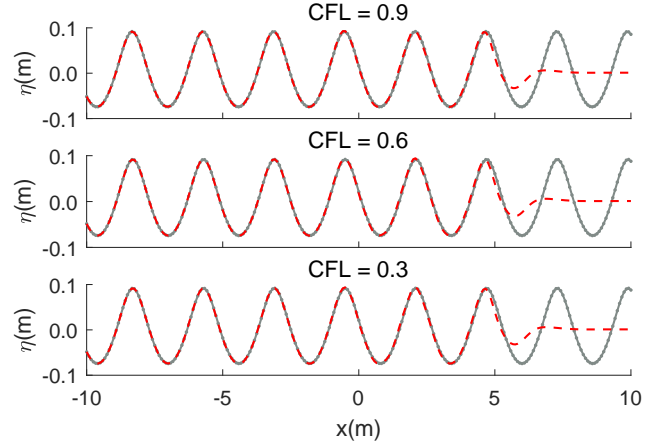
654 Four regular waves with different steepness shown in Table 3 are considered, where  $H$  is the  
655 wave height,  $T$  is the wave period,  $k$  is the wave number and  $ka$  with  $a = H/2$  representing the  
656 non-linearity of the waves. The  $CFL$  number is defined as  $CFL = c\Delta t/\Delta x$ , where  $c$  is the wave  
657 phase velocity,  $\Delta t$  is time step and  $\Delta x$  the grid spacing in the deepest grid level. In Table 3, the  
658 steepest wave with  $ka = 0.4$  is quite close to the deep-water breaking wave limit.

659 In order to test the performance of the wave tank, the wave elevation for  $ka = 0.1 \sim 0.4$  are  
660 plotted together with the stream-function solution at the time instant  $t = 20s$  in Fig. 21. In Table 3,  
661 Case-1 and Case-3 are used to investigate the influence of grid refinement on the numerical solutions,  
662 while Case-2 and Case-4 are designed to study the influence of different time steps.

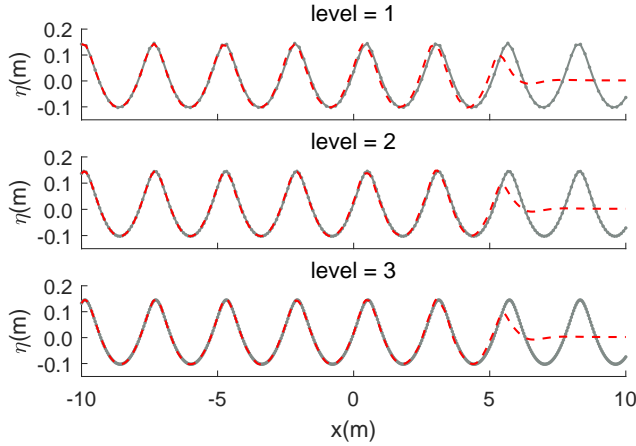
663 As shown in Fig. 21(a), there is an excellent agreement between the numerical and reference  
664 solutions outside of the damping zone for  $ka = 0.1$  with different grid refinements. As the wave



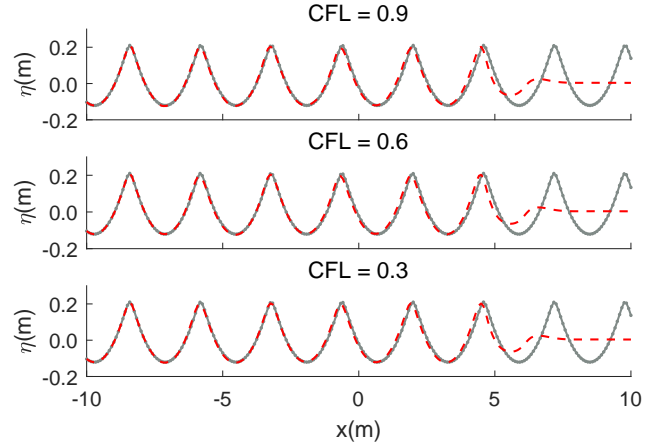
(a)  $ka = 0.1$ ,  $CFL = 0.5$



(b)  $ka = 0.2$ ,  $level = 2$



(c)  $ka = 0.3$ ,  $CFL = 0.5$



(d)  $ka = 0.4$ ,  $level = 2$

Figure 21: Wave profile for waves in Table 3. Present numerical results are compared with analytical solution provided by Rienecker and Fenton [68].

665 steepness increases to  $ka = 0.3$ , we notice an obvious phase lag for a level-1 mesh, due to the  
 666 dispersion error introduced by the numerical solution. A finer grid, e.g.  $level_{\max} = 2$  or 3, can  
 667 significantly reduce the dispersion error. In general, the moderate grid refinement ( $level_{\max} = 2$ )  
 668 with 32 nodes per wave length is sufficient to provide an accurate simulation for wave steepness up  
 669 to  $ka = 0.3$ . If we fix the grid spacing and use  $level_{\max} = 2$  for Case-2 and Case-4, it is seen from  
 670 Fig. 21(b) and (d) that all time steps are sufficient as long as  $CFL \leq 1$  thanks to the 4<sup>th</sup>-order time-  
 671 integration method. Strong nonlinearity of waves increases the challenge of computational modeling,  
 672 and that is why the dispersion error looks more evident for Case-4 with moderate mesh resolution  
 673 (i.e.  $level_{\max} = 2$ ) than for the other cases. Therefore the Savitsky-Golay (SG) filter by Savitzky and  
 674 Golay [75] with 13 points and 10<sup>th</sup> order is applied to smooth the wave elevation and the velocity  
 675 potential at each time step. It should be noted that the SG filter is only used for Case-4, not for the  
 676 other cases in Table 3.

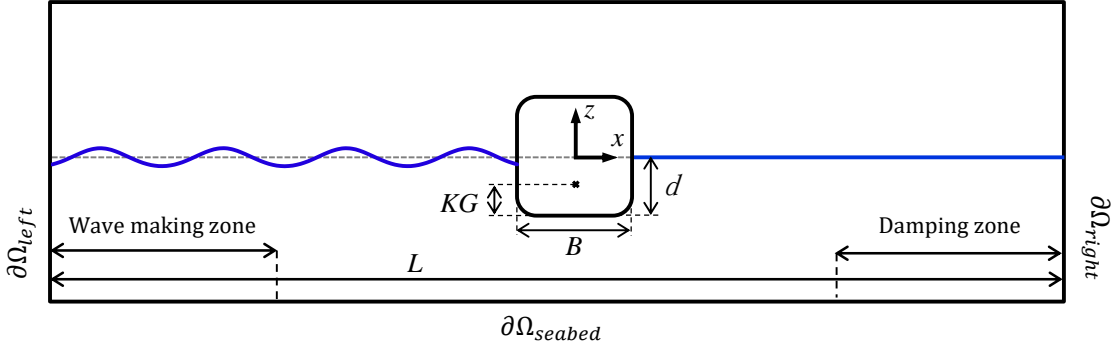


Figure 22: Sketch of a fixed semi-submerged barge in regular waves.

## 6.2 Fixed barge section in regular waves

The developed 2D fully-nonlinear numerical wave tank is utilized to analyze a wave-diffraction problem, with a fixed surface-piercing barge in regular waves with various wave heights and frequencies. The wave loads on the barge were studied theoretically by Maruo [76], experimentally by Nojiri [77] and by Koo [78], Tanizawa [79] and Hanssen [47] using fully-nonlinear potential flow analyses. Fig. 22 shows the layout of the numerical wave tank. The length of the tank is set to be  $L = 8L_w$  and the water depth is  $h = L_w$ , where  $L_w$  is the wavelength. Waves are generated by the wave making zone described in § 6.1. It also acts as a damping zone, absorbing the reflected waves from the barge, which avoids undesirable wave reflection back and forth between the left boundary and the barge. The length of both the wave making zone and the wave damping zone are taken as  $L_{WMMZ} = L_{WDDZ} = 2L_w$ . The center of this barge is coincident with the origin of a global Cartesian coordinate system  $Oxz$ , with the origin at middle of the tank,  $x$ -axis pointing positively along the direction of wave propagating and  $z$ -axis pointing vertically upwards. The characteristic geometric parameters of the barge are chosen the same as the experiment from [77], with a breadth  $B = 0.5m$ , a draught  $d = B/2$ , a round corner radius  $r = 0.064m$  and a gravitational height  $KG = 0.135m$ .

As in [79], incident regular waves with two different wave heights  $H = 0.01m$  and  $H = 0.07m$  are used. To generate the waves in the wave making zone, we have used both linear waves and nonlinear stream-function incident waves as used in § 6.1 as inputs in Eq. (42). In case a linear incident wave solution is used, the generated wave outside of the wave making zone will still develop into a fully-nonlinear wave. The non-dimensional wave frequency  $\xi_B = \omega^2 B/2g$  ranging from 0.25 to 2.00 are simulated, where  $\omega$  is angular wave frequency and  $g$  denotes gravitational acceleration. The wave frequencies and other important parameters, including the wave lengths  $L_w^l$  and  $L_w^{sf}$  calculated by a linear wave theory and stream function theory respectively, the wave period  $T$  and the wave steepness  $ka$ , where  $k$  is the wave number and  $a$  is the wave amplitude defined as  $a = H/2$ , are listed in Table 4. For all cases in Table 4, a time step  $T/\Delta t$  from 40 to 100 is used from the lowest to the highest frequencies. The grid spacing at the deepest grid level is subject to the criterion  $dx = dz = \min(B/14, L_w/30)$ . The ramp time for wave making is set to be  $t_{ramp} = 4T$ . Wave markers here will be subjected to the fully Lagrangian free-surface kinematic and dynamic boundaries conditions, uniformly distributed along the  $x$ -axis. The explicit RK4 time scheme is used to integrate the Lagrangian time derivative of the positions and velocity potential of wave markers.

The time history of non-dimensional forces along the  $x$ -axis (sway force) and  $z$ -axis (heave force) and the moment around the  $y$ -axis (roll moment) on the barge section for linear waves with wave

Table 4: Definition of periodic waves for a fixed barge in waves.

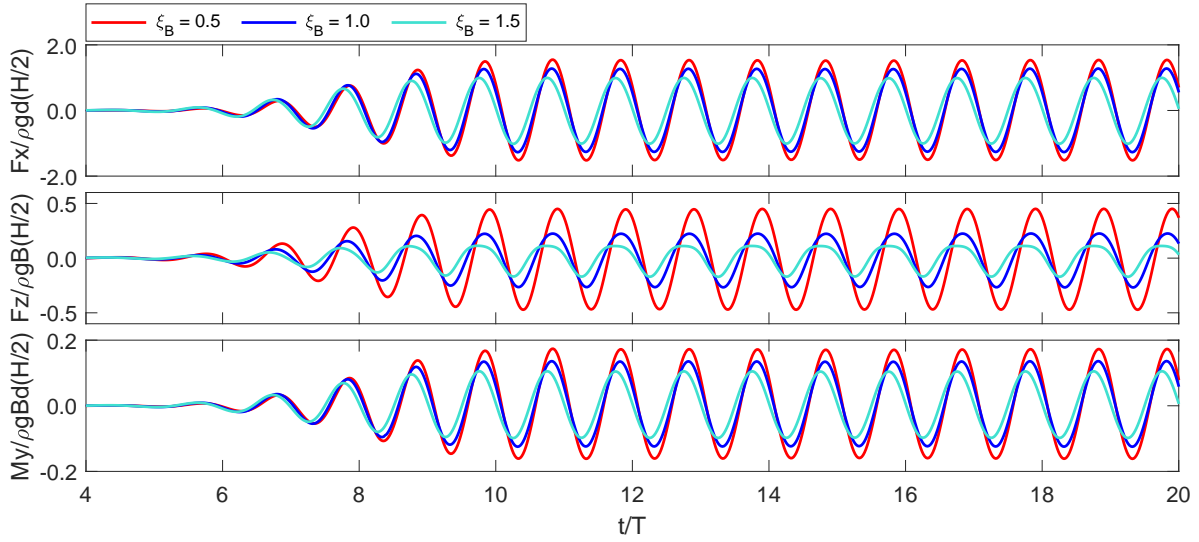
| $\xi_B$ | $\omega(s^{-1})$ | $L_w^l(m)$ | $L_w^{sf}(m)$ | $T(s)$ | $ka_{H=1cm}$ | $ka_{H=7cm}$ |
|---------|------------------|------------|---------------|--------|--------------|--------------|
| 0.250   | 3.132            | 6.283      | 6.288         | 2.006  | 0.005        | 0.035        |
| 0.500   | 4.429            | 3.142      | 3.159         | 1.419  | 0.010        | 0.070        |
| 0.550   | 4.645            | 2.856      | 2.874         | 1.353  | 0.011        | 0.077        |
| 0.600   | 4.851            | 2.618      | 2.638         | 1.295  | 0.012        | 0.084        |
| 0.650   | 5.049            | 2.417      | 2.439         | 1.244  | 0.013        | 0.091        |
| 0.700   | 5.240            | 2.244      | 2.270         | 1.199  | 0.014        | 0.098        |
| 0.750   | 5.424            | 2.094      | 2.118         | 1.158  | 0.015        | 0.105        |
| 1.000   | 6.263            | 1.571      | 1.601         | 1.003  | 0.020        | 0.140        |
| 1.250   | 7.002            | 1.257      | 1.294         | 0.897  | 0.025        | 0.175        |
| 1.500   | 7.671            | 1.047      | 1.091         | 0.819  | 0.030        | 0.210        |
| 1.750   | 8.285            | 0.898      | 0.948         | 0.758  | 0.035        | 0.245        |
| 2.000   | 8.857            | 0.785      | 0.841         | 0.709  | 0.040        | 0.280        |

709 height  $H = 0.01m$  and  $H = 0.07m$  are shown in Fig. 23, where non-dimensional frequencies  $\xi_B =$   
710  $(0.5, 1.0, 1.5)$  are chosen to display. Only 20 wave periods are shown since the simulation reaches  
711 steady state after approximate  $t/T = 10$ . Nonlinear features clearly increase as the incident wave  
712 frequency grows, particularly for the heave force in short waves. We can see from Table 4 that the  
713 largest wave steepness is  $ka = 0.28$ . When this incident wave reaches the barge, partially standing  
714 waves are expected on the weather side of the barge, in particular for shorter incident waves due to  
715 stronger wave diffraction, leading to higher nonlinearities. In order to suppress numerical instabilities,  
716 a non-centered selective filter is applied near the wave-body intersection waterline [80], while a 13-  
717 points and 10<sup>th</sup>-order SG filter is again used for the free surface away from the body [75, 81]. This  
718 combination of mixed filters is also used for other wave-body intersection problems in the following  
719 applications.

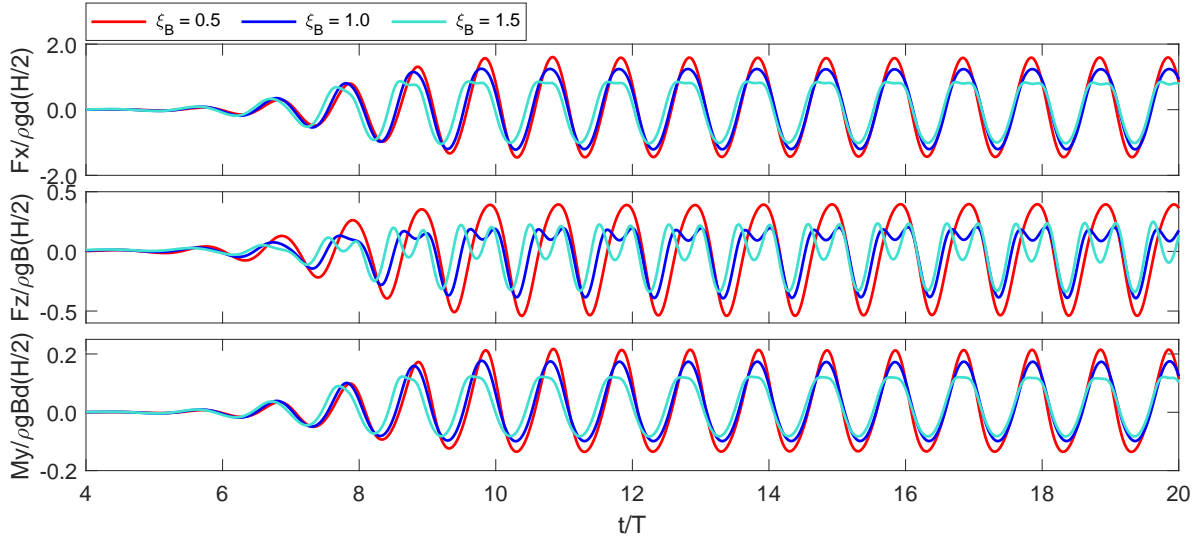
720 A Fourier analysis of the time series of the load  $F(t)$  on the barge is conducted as

$$F(t) = a_0 + \sum_{n=1}^N (a_n \cos(n\omega t) + b_n \sin(n\omega t)), \quad (44)$$

721 where  $a_n$  and  $b_n$  can be calculated by a least squares fit to a steady-state portion of the time-series.  
722 Here the  $n$ -th order load is calculated as  $F^{(n\omega)} = \sqrt{a_n^2 + b_n^2}$  and  $a_0$  denotes the mean wave load. In  
723 the present study, the last 5 periods of the time histories are taken to perform the Fourier analysis.  
724 Fig. 24 shows the normalized sway mean-drift force  $F_x^{(0)}$ , the first harmonics of the sway force  $F_x^{(1\omega)}$ ,  
725 heave force  $F_z^{(1\omega)}$  as well as roll moment  $M_y^{(1\omega)}$  on the fixed barge. The present results of linear  
726 waves with wave height  $H = 0.01m$  and  $H = 0.07m$  and nonlinear with wave height  $H = 0.07m$   
727 are compared with theoretical solution from [76] based on a perturbation method, experimental  
728 results of [77] and fully-nonlinear numerical analysis of  $H = 0.07m$  from [79] using linear waves as  
729 input signal. Note that all the wave forces are obtained through direct pressure integration along  
730 the wetted surface of the barge. The present results are generally in good agreement with the  
731 analytical solutions, numerical results of [79] and experimental results, despite some deviations at  
732 high frequencies from the experiments. The force results by the linear wave theory and the stream  
733 function theory are compared in Fig. 24. Although the input wave signals are different, the difference



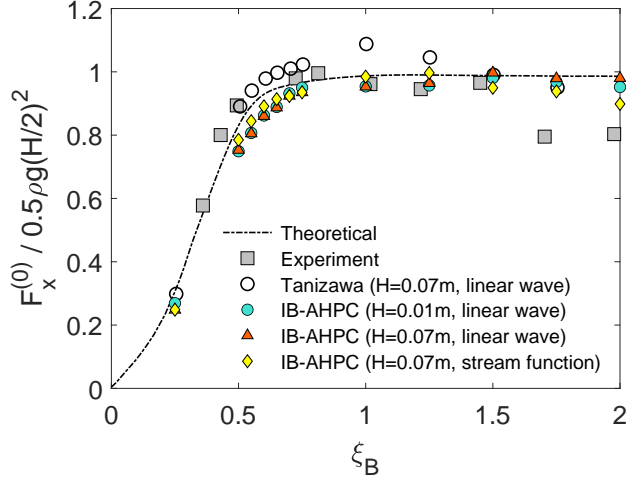
(a) Wave height  $H = 0.01\text{m}$



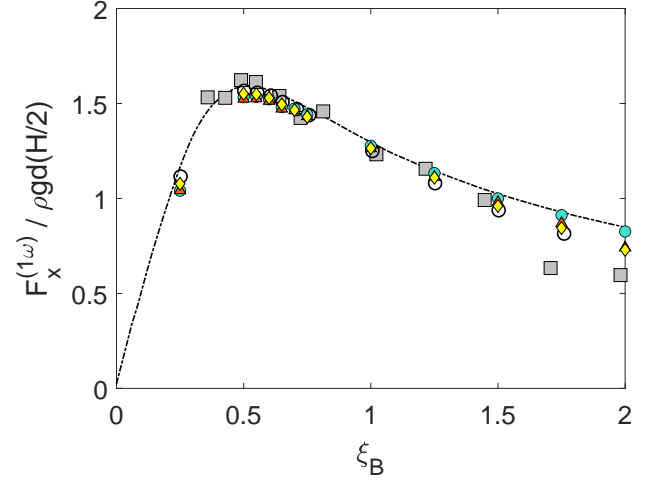
(b) Wave height  $H = 0.07\text{m}$

Figure 23: Non-dimensional force history for a fixed semi-submerged barge in waves by linear wave theory for wave height  $H = 0.01\text{m}$  and  $H = 0.07\text{m}$  with non-dimensional wave frequency  $\xi_B = 0.5, 1.0, 1.5$ .

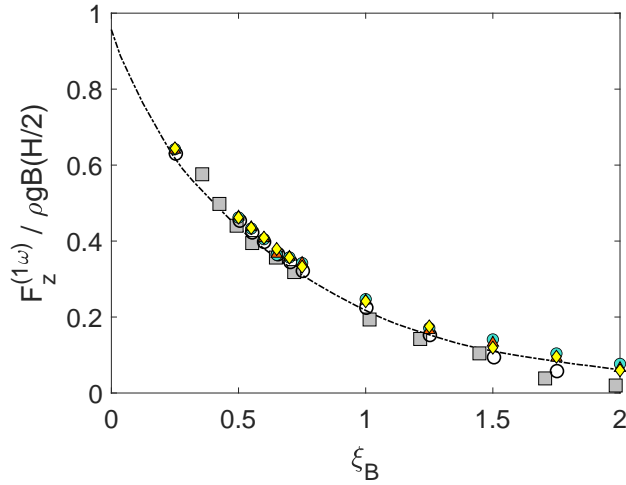
734 of the results by linear and nonlinear waves with  $H = 0.07\text{m}$  is not obvious, except for the mean  
 735 sway drift force at frequency  $\xi_B = 2.0$ . When the stream function theory is applied in the wave  
 736 making zone, our numerical results tend to share a similar tendency as that in the experiment [77],  
 737 i.e. the non-dimensional mean sway drift force  $F_x^{(0)}$  tend to decrease as the frequency increases. The  
 738 deviation from the theoretical solution might be due to the strong non-linearity of waves at higher  
 739 frequencies. Since a fixed wave height is considered for all frequencies, the non-linearity increases  
 740 with frequency, which can be understood from the  $ka$  values in Table 4. In the low frequency region,  
 741 both the results of  $H = 0.01\text{m}$  and  $H = 0.07\text{m}$  for  $F_x^{(0)}$ ,  $F_x^{(1\omega)}$  and  $F_z^{(1\omega)}$  are very close to each other.



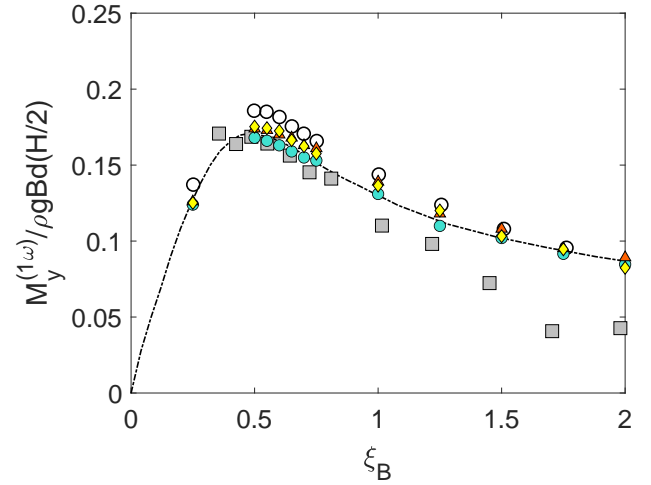
(a) Mean sway drift force



(b) Sway force



(c) Heave force



(d) Roll moment

Figure 24: Normalized first harmonic component wave exciting forces and the mean sway drift force on the fixed barge. Present numerical results by linear waves ( $H = 0.01m$  and  $H = 0.07m$ ) and nonlinear waves by the stream function theory ( $H = 0.07m$ ) are compared with theoretical linear solution from [76], experimental solution from [77] and numerical results from [79].

### 742 6.3 Forced heaving of a 2D Lewis-form barge section in still water

743 The radiation problem of a Lewis-form barge harmonically heaving on the free surface is con-  
 744 sidered here to test the capability of the numerical model on simulating the wave-body interaction.  
 745 Fig. 25 gives a snapshot of an adaptive grid system with  $level_{\max} = 2$  and  $e\text{-degree} = 2$  for this  
 746 heaving barge section in a numerical wave tank. Some colored nodes with different node types can  
 747 be referred from § 3.2 and § 4.2. In this part, the breadth of the Lewis-form barge is kept the same  
 748 as in § 6.2 and the block coefficient of this Lewis-form section is defined as  $\epsilon = S/(Bd) = 0.989$ .  
 749 The length of the wave tank is  $L = 8L_w$  and the water depth here is  $h = \max(L_w, 3B)$ . The  
 750 wave making zone is changed into a damping zone and the length of the damping zone at left  
 751 and right end of this tank is  $L_{WDZ} = 2L_w$ . The initial draught of the barge is also set to be

752  $d = B/2$ . The heave motion is given as  $\eta_{heave}(t) = \eta_a \sin \omega t$ , and the non-dimensional heaving am-  
753 plitude is defined as  $\sigma_{heave} = \eta_a/(B/2) = 0.222$ . In order to achieve a good accuracy close to the  
754 wave-body intersection point, we have used a grid size in the deepest level based on the criterion  
755  $dx = dz = \min(B/25, L_w/40)$ . A time step of  $T/\Delta t = 40$  is chosen for all frequencies. The main  
756 properties of the waves generated by the heaving motion of the barge are summarized in Table 5,  
757 which are based on linear dispersion relationship. The ramp time to gradually start the motion is  
758 set as  $t_{ramp} = 4T$  and the simulation time is  $t_{sim} = 10T$  for each case listed in Table 5. A Fourier  
759 analysis is performed on the time history of heaving force on the barge using Eq. (44). Then the  
760 added mass  $A_{33}$  and damping coefficients  $B_{33}$  can be found from the first harmonic components,

$$A_{33} = -\frac{b_{3,1} - C_z \eta_a}{\omega^2 \eta_a}, \quad B_{33} = \frac{a_{3,1}}{\omega \eta_a}, \quad (45)$$

761 where the hydrostatic restoring coefficient is given as  $C_{33} = \rho g B$ .

Table 5: Definition of periodic waves generated by a harmonically heaving barge in undisturbed water.

| $\xi_B$ | $\omega(s^{-1})$ | $L_w(m)$ | $T(s)$ | $h(m)$ |
|---------|------------------|----------|--------|--------|
| 0.250   | 3.132            | 6.283    | 2.006  | 6.283  |
| 0.500   | 4.429            | 3.142    | 1.419  | 3.142  |
| 0.750   | 5.424            | 2.094    | 1.158  | 2.094  |
| 1.000   | 6.263            | 1.571    | 1.003  | 1.571  |
| 1.200   | 6.862            | 1.309    | 0.916  | 1.500  |
| 1.500   | 7.671            | 1.047    | 0.819  | 1.500  |
| 1.750   | 8.285            | 0.898    | 0.758  | 1.500  |
| 2.000   | 8.857            | 0.785    | 0.709  | 1.500  |

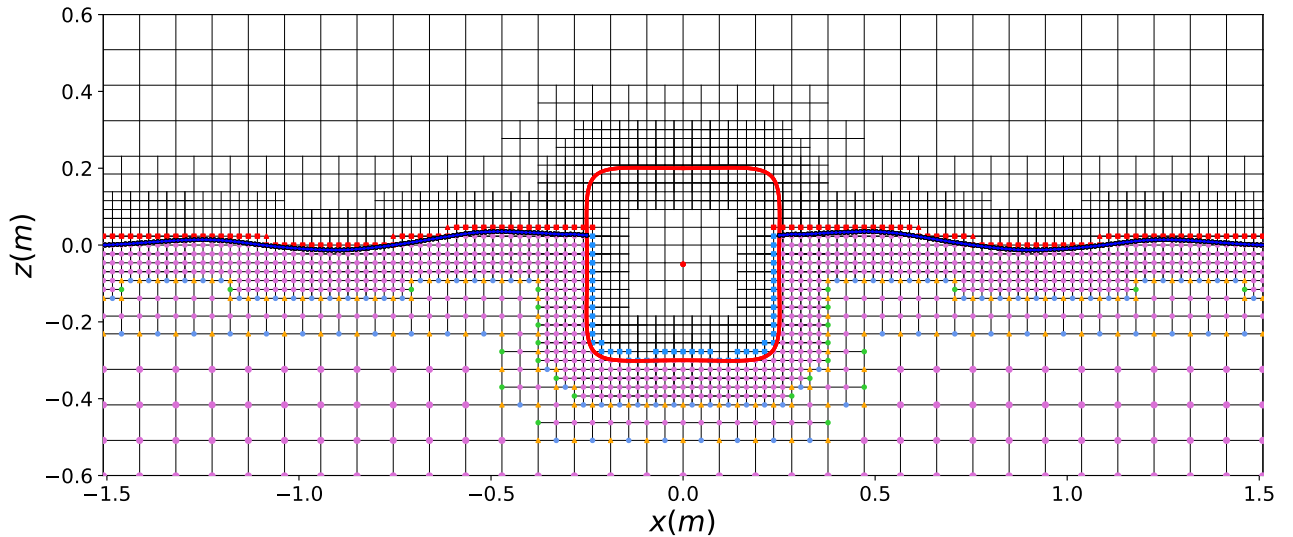


Figure 25: Adaptive Cartesian grid system for a forced heaving Lewis-form barge at free surface.  $level_{max} = 2$  and  $e-degree = 2$

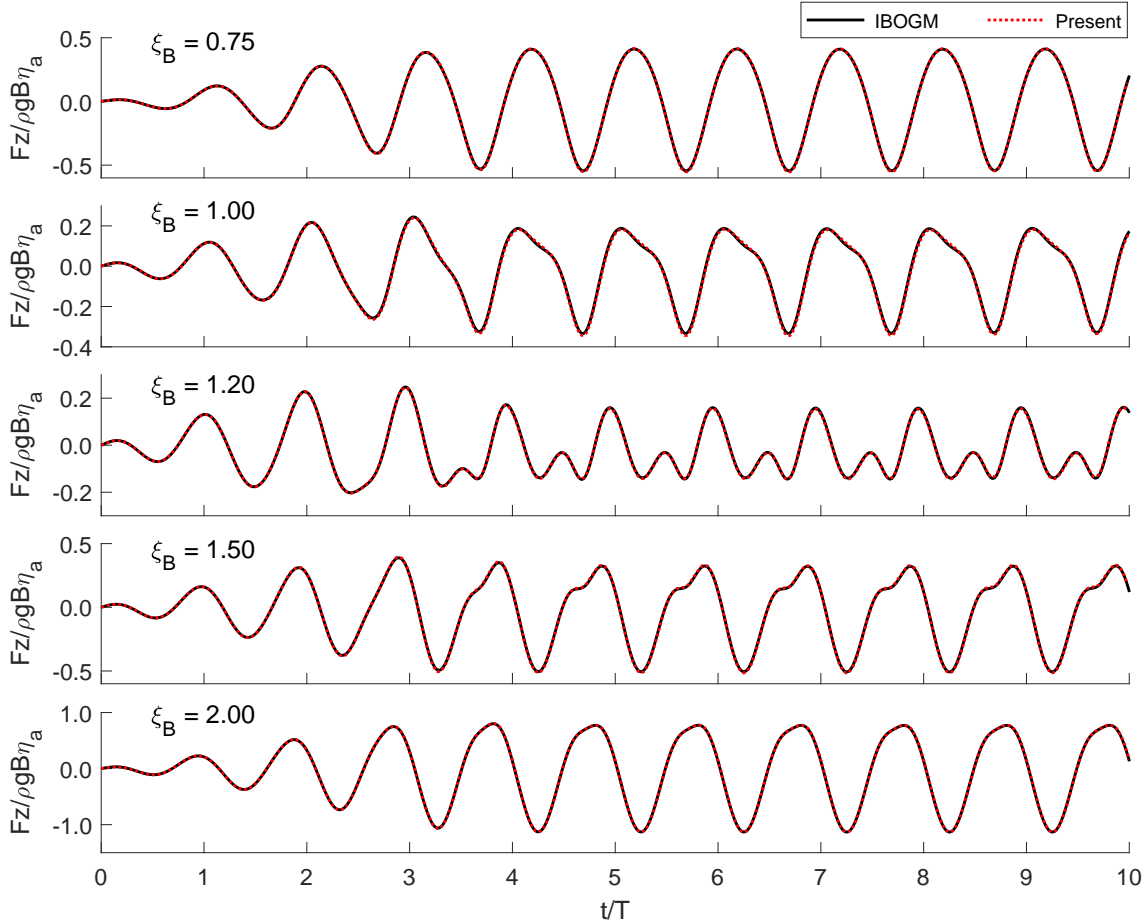
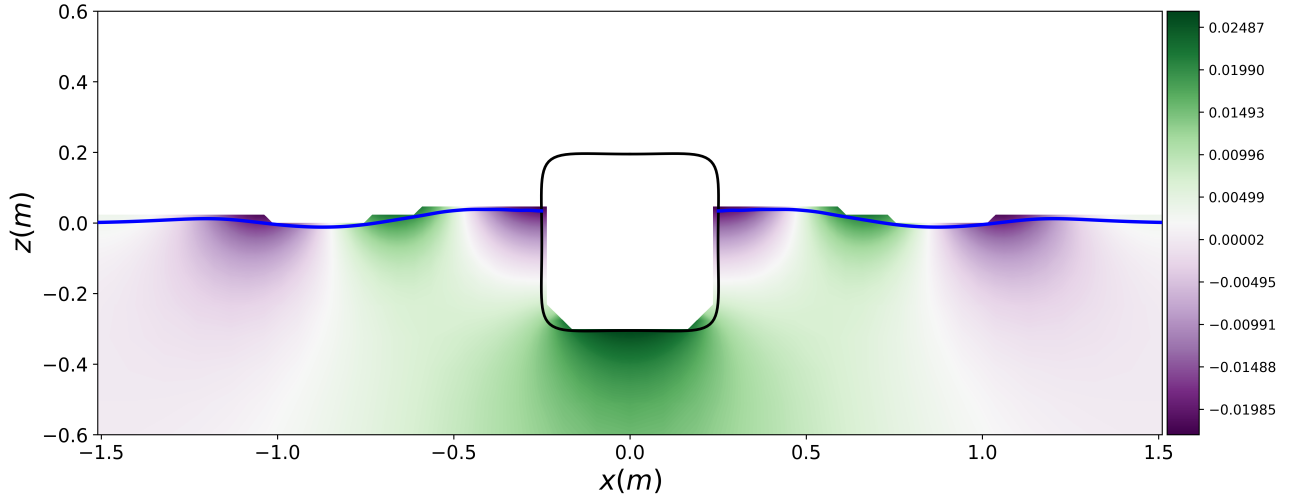


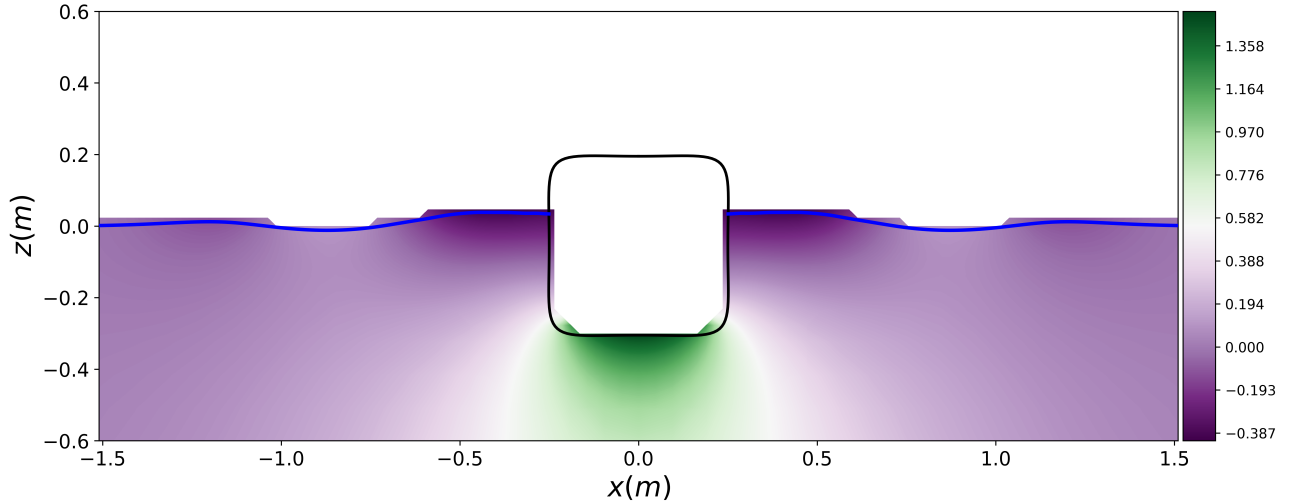
Figure 26: Time history of normalized heaving force (excluding restoring force) of a harmonic heaving barge for frequency  $\xi_B = (0.75, 1.00, 1.20, 1.50, 2.00)$ . Present work on time history of heaving force is compared with the numerical reference from the IBOGM in [47].

762 Fig. 26 shows the time history of normalized heaving forces on the barge for five different frequen-  
763 cies  $\xi_B = (0.75, 1.00, 1.20, 1.50, 2.00)$ . Our present results are compared with another fully-nonlinear  
764 HPC solver based on Immersed Boundary-Overlapping Grid Method (IBOGM) [47], providing refer-  
765 ence results in the form of time series. The IBOGM has been carefully verified and validated as  
766 a highly accurate method in [51] and [47]. Based on direct comparison of time series, the present  
767 results and the IBOGM are visually in perfect agreement. The time series effectively prove that  
768 there are no spurious oscillations by applying the Lagrangian acceleration potential method (LAPM)  
769 described in § 3.3 to evaluate  $\partial\varphi/\partial t$ . Fig. 27 displays the field distribution of the velocity potential  
770  $\varphi$  and the Lagrangian acceleration potential  $\Psi$  at  $t = \frac{1}{4}T$  for a Lewis-form barge section heaving at  
771 the free surface at a frequency  $\xi_B = 2.00$ . It is clear to see the continuity of the field for both  $\varphi$  and  
772  $\Psi$ , which contributes to the smoothness of the force signals in Fig. 26 by applying the LAPM.

773 Using an IBM combined with a finite-difference method to estimate the time derivative of the  
774 velocity potential in analyses with moving bodies, inevitably leads to spurious pressure- and force  
775 oscillations [49]. Another way to evaluate  $\varphi_t$  in the Bernoulli's equation is the Eulerian acceleration  
776 potential method (EAPM). See, e.g. [59] and [58], and a short description in § 3.3. In Fig. 28, the



(a)  $\varphi$ ,  $t = \frac{1}{4}T$



(b)  $\Psi$ ,  $t = \frac{1}{4}T$

Figure 27: Field distribution of (a) the velocity potential  $\varphi$  and (b) the Lagrangian acceleration potential  $\Psi$  at  $t = \frac{1}{4}T$  for a Lewis-form barge harmonically heaving at free surface at the non-dimensional frequency  $\xi_B = 2.00$ .  $level_{\max} = 2$  and  $e\text{-degree} = 2$ .

777 results of time history of heaving force for two selected frequencies  $\xi_B = (1.20, 2.00)$  by using the  
 778 EAPM and LAPM in the present analysis are compared. Here, the grid refinement, using the EAPM  
 779 and LAPM, for one specific frequency is kept the same. In our numerical experiments, we found that  
 780 even if we apply the EAPM from [59], we still cannot get the time history of force as smooth as that  
 781 by the LAPM. It also turns out that the EAPM performs worse for cases with stronger nonlinearities.  
 782 Although the result from the EAPM tends to improve with weaker nonlinearities, it is still not as  
 783 good as the LAPM. The difference can be explained by the second-order spatial derivative term  
 784 of the velocity potential in the Neumann boundary conditions in Eq. (20) for the EAPM, which is  
 785 challenging to estimate accurately, especially for where the gradient of velocity changes strongly. The  
 786 LAPM, however, does not involve any derivatives in the body boundary condition. See Eq. (25).

787 The present results of added mass and damping coefficients as well as 1<sup>st</sup>-order heave forces are

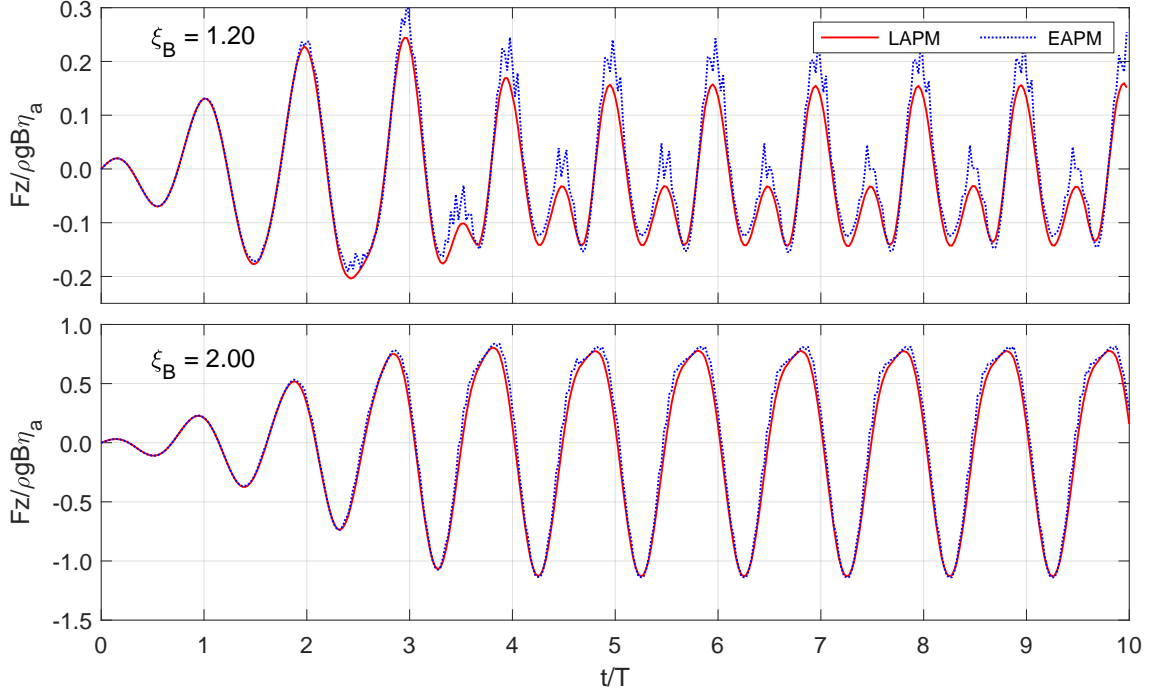


Figure 28: Time history of normalized heaving force (excluding restoring force) of a harmonic heaving barge for frequency  $\xi_B = (1.20, 2.00)$ , using the EAPM and LAPM, respectively, to estimate the time derivative of the velocity potential.

788 compared with linear analytical solutions and experimental measurements from Tasai and Koterayama [82], fully-nonlinear BEM results of Grytøyrr [83] and numerical solutions from IBOGM by  
789 Hanssen [47], as shown in Figure 29. The consistence are fairly satisfactory. For the 1<sup>st</sup>-order force,  
790 present results are pretty in agreement with the fully nonlinear results of [83] and [47]. Tasai and  
791 Koterayama [82] have also presented the 2<sup>nd</sup>-order force component in two different ways: the nor-  
792 malized force amplitudes and the ratio of the 2<sup>nd</sup>-order to the 1<sup>st</sup>-order force amplitudes. They also  
793 gave the ratio for the 3<sup>rd</sup>-order to the 1<sup>st</sup>-order force amplitudes, but no normalized experimental  
794 results of the 3<sup>rd</sup>-order force were presented. Here, our present numerical results of higher order  
795 force components are compared with experimental results of [82], fully-nonlinear BEM results of [83]  
796 and numerical results of IBOGM from [47], as shown in Figure 30. We can notice that, despite of  
797 slightly deviations comparing to the BEM and the IBOGM for the 2<sup>nd</sup>- and 3<sup>rd</sup>-order force in the high  
798 frequency region, generally speaking, the present results match well with reference solutions. It is  
799 not clear how large uncertainties are in the experiments, in particular for the 3<sup>rd</sup>-order forces at high  
800 frequencies, which is known to be challenging to measure accurately in model-scale experiments. The  
801 experimental results show that the 3<sup>rd</sup> force component is much larger than the 2<sup>nd</sup>-order component  
802 at  $\xi_B = 1.8$ , while none of the presented numerical results are able to reproduce this.  
803

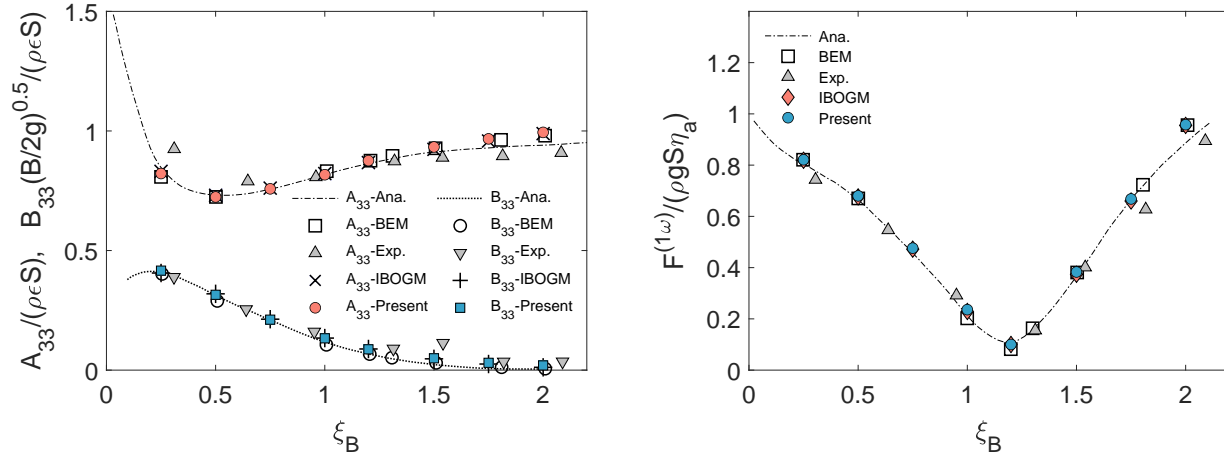


Figure 29: Heaving added mass and damping coefficients and normalized first-order Fourier force-component for a Lewis-form barge. Here  $S = Bd$  is the mean submerged area of the barge.

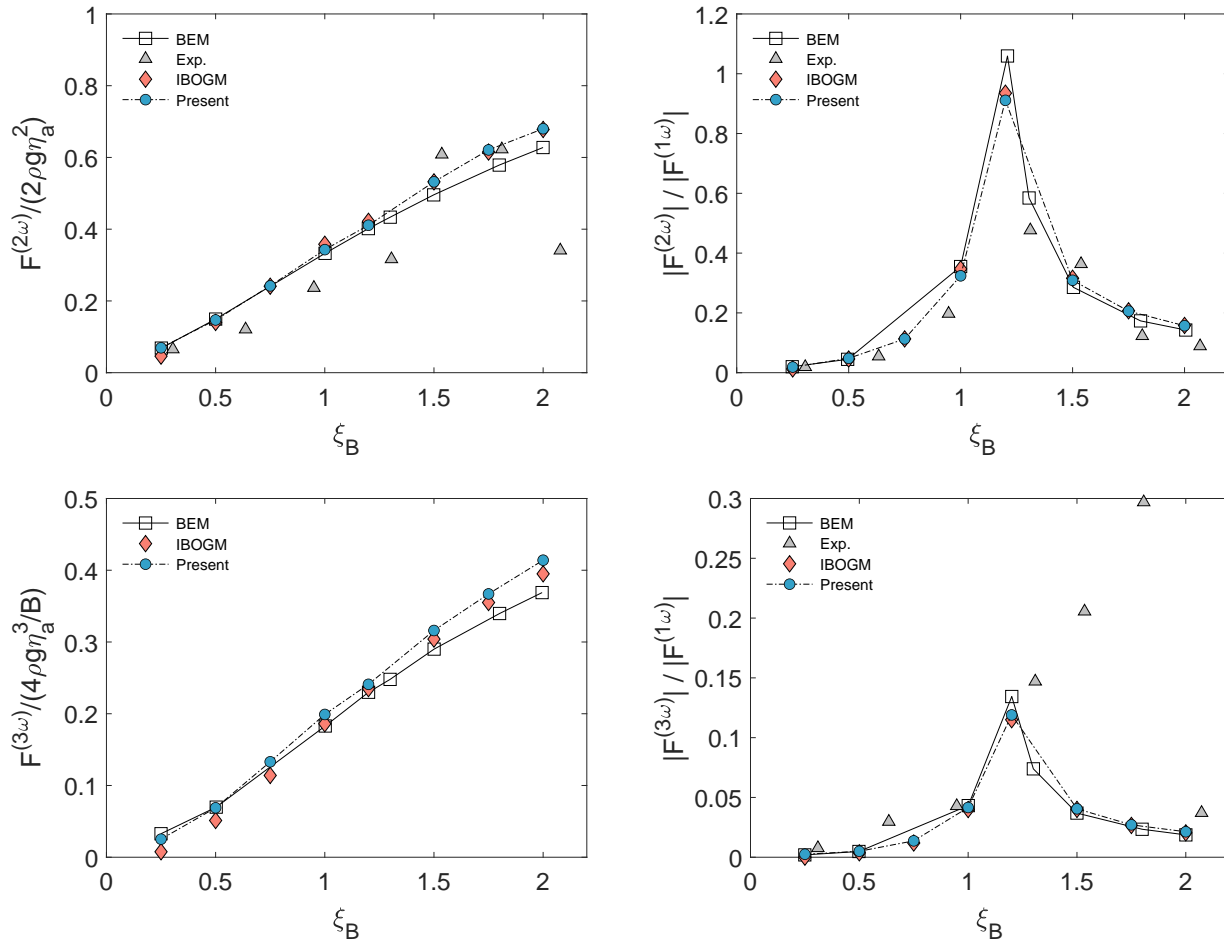


Figure 30: 2<sup>nd</sup>-order and 3<sup>rd</sup>-order heaving force coefficients (left column), and ratio of 2<sup>nd</sup>-order and 3<sup>rd</sup>-order force amplitude to 1<sup>st</sup>-order force amplitude (right column), respectively, for a heaving Lewis-form barge.

## 804 7 Conclusion

805 In this paper, a highly accurate and efficient 2D Harmonic Polynomial Cell method has been  
806 developed based on adaptive Cartesian quad-tree cells and the immersed boundary strategy to solve  
807 the Laplace equation. The adaptive cells ensure local grid refinement in places of interest, such as at  
808 the free surface and regions near moving structures, leading to a significant savings in computational  
809 effort without sacrificing accuracy compared to a strategy where the entire grid is refined uniformly.  
810 For a circular cylinder in an infinite fluid, the total number of grid points required to reach a given  
811 accuracy is found to scale with  $(1/\Delta x)^{0.8\sim 0.9}$  compared to  $(1/\Delta x)^2$  for a method without local grid  
812 refinement. The method also avoids using irregular cells [25, 84] to handle complex geometries.  
813 Instead, standard square cells are used everywhere, making the implementation of the method very  
814 straightforward.

815 A matrix-based stability analysis of the adaptive grid for the present IB-AHPC method is car-  
816 ried out, to our knowledge, for the first time since the HPC method was proposed by Shao and  
817 Faltinsen[24]. We have used the stability analysis results as a guide when designing the numerical  
818 schemes, especially the treatment of Neumann boundary conditions, which are essential to the sta-  
819 bility of the scheme. The analysis for stretched cells also reveals that the mesh aspect ratio  $\Delta z/\Delta x$   
820 has a strong influence on stability, and that square cells have the best stability properties. Since  
821 square cells have also been shown to have the best accuracy [45], the use of square cells is strongly  
822 encouraged as optimum from both an accuracy and a stability point of view.

823 The spurious force oscillations for moving structures, which have been reported in the literature  
824 for immersed boundary methods (IBMs), are eliminated in this study by solving a separate boundary  
825 value problem (BVP) for a Lagrangian acceleration potential. Solving the corresponding Eulerian  
826 acceleration potential is shown to be far less satisfactory due to the involved second derivatives of  
827 the velocity potential in the body-boundary condition. These are challenging to estimate accurately  
828 in general, and especially in an IBM-based approach.

829 Various fully-nonlinear potential flow problems have been studied to demonstrate the accuracy  
830 and capability of the numerical model, including generation of periodic waves up to near breaking  
831 in a nonlinear water wave tank, nonlinear diffraction by a fixed ship section in regular waves, and  
832 nonlinear radiation by the forced heave motion of a Lewis-form barge in still water. The excellent  
833 agreement with numerical and experimental references suggests that the present method is capable  
834 of treating fully-nonlinear wave-structure interaction problems in an accurate and computationally  
835 efficient way, which can be readily extended to 3D.

## 836 Acknowledgment

837 The first author (C. Tong) is mainly fund-supported by the Chinese Scholarship Council (No.  
838 201906230317). This work is carried out at Fluid mechanics, Coastal and Maritime Engineering,  
839 Department of Mechanical Engineering in DTU. The fourth author is funded by the Centre for  
840 Autonomous Marine Operations and Systems (AMOS). The Research Council of Norway (Norges  
841 Forskningsråd) is acknowledged as the main sponsor of AMOS. This work was supported by the  
842 Research Council of Norway through the Centre of Excellence funding scheme, Project number  
843 223254-AMOS.

## References

- 845 [1] Chorin AJ. Numerical solution of the Navier-Stokes equations. *Mathematics of computation*.  
846 1968;22(104):745–762.
- 847 [2] Taylor C, Hood P. A numerical solution of the Navier-Stokes equations using the finite element  
848 technique. *Computers & Fluids*. 1973;1(1):73–100.
- 849 [3] Jacobsen NG, Fuhrman DR, Fredsøe J. A wave generation toolbox for the open-source CFD  
850 library: OpenFoam®. *International Journal for numerical methods in fluids*. 2012;70(9):1073–  
851 1088.
- 852 [4] Higuera P, Lara JL, Losada IJ. Realistic wave generation and active wave absorption for Navier–  
853 Stokes models: Application to OpenFOAM®. *Coastal Engineering*. 2013;71:102–118.
- 854 [5] Hu ZZ, Greaves D, Raby A. Numerical wave tank study of extreme waves and wave-structure  
855 interaction using OpenFoam®. *Ocean Engineering*. 2016;126:329–342.
- 856 [6] Bihs H, Kamath A, Chella MA, Aggarwal A, Arntsen ØA. A new level set numerical wave tank  
857 with improved density interpolation for complex wave hydrodynamics. *Computers & Fluids*.  
858 2016;140:191–208.
- 859 [7] Kamath A, Bihs H, Alagan Chella M, Arntsen ØA. Upstream-cylinder and downstream-cylinder  
860 influence on the hydrodynamics of a four-cylinder group. *Journal of waterway, port, coastal,  
861 and ocean engineering*. 2016;142(4):04016002.
- 862 [8] Oggiano L, Pierella F, Nygaard TA, De Vaal J, Arens E. Reproduction of steep long crested  
863 irregular waves with CFD using the VOF method. *Energy Procedia*. 2017;137:273–281.
- 864 [9] Kim SY, Kim KM, Park JC, Jeon GM, Chun HH. Numerical simulation of wave and current  
865 interaction with a fixed offshore substructure. *International Journal of naval Architecture and  
866 ocean engineering*. 2016;8(2):188–197.
- 867 [10] Tavelli M, Dumbser M. A staggered space–time discontinuous Galerkin method for the incom-  
868 pressible Navier–Stokes equations on two-dimensional triangular meshes. *Computers & Fluids*.  
869 2015;119:235–249.
- 870 [11] Fambri F, Dumbser M. Spectral semi-implicit and space–time discontinuous Galerkin methods  
871 for the incompressible Navier–Stokes equations on staggered Cartesian grids. *Applied Numerical  
872 Mathematics*. 2016;110:41–74.
- 873 [12] Fambri F, Dumbser M. Semi-implicit discontinuous Galerkin methods for the incompressible  
874 Navier–Stokes equations on adaptive staggered Cartesian grids. *Computer Methods in Applied  
875 Mechanics and Engineering*. 2017;324:170–203.
- 876 [13] Dumbser M, Fambri F, Furci I, Mazza M, Serra-Capizzano S, Tavelli M. Staggered discontin-  
877 uous Galerkin methods for the incompressible Navier–Stokes equations: Spectral analysis and  
878 computational results. *Numerical Linear Algebra with Applications*. 2018;25(5):e2151.
- 879 [14] Dean RG, Dalrymple RA. *Water wave mechanics for engineers and scientists*. vol. 2. World  
880 Scientific Publishing Company; 1991.
- 881 [15] Ramming HG, Kowalik Z. *Numerical modelling of marine hydrodynamics*. Elsevier; 1980.
- 882 [16] Faltinsen O. *Sea loads on ships and offshore structures*. vol. 1. Cambridge university press;  
883 1993.
- 884 [17] Grilli ST, Skourup J, Svendsen IA. An efficient boundary element method for nonlinear water  
885 waves. *Engineering Analysis with Boundary Elements*. 1989;6(2):97–107.

- 886 [18] Grilli S. Fully nonlinear potential flow models used for long wave runup prediction. Chapter in  
887 Long-Wave Runup Models,(eds H Yeh, P Liu, and C Synolakis). 1997;p. 116–180.
- 888 [19] Ferrant P, Touzé DL, Pelletier K. Non-linear time-domain models for irregular wave diffraction  
889 about offshore structures. *International journal for numerical methods in fluids*. 2003;43(10-  
890 11):1257–1277.
- 891 [20] Bai W, Teng B. Simulation of second-order wave interaction with fixed and floating structures  
892 in time domain. *Ocean engineering*. 2013;74:168–177.
- 893 [21] Harris JC, Dombre E, Benoit M, Grilli ST, et al. Fast integral equation methods for fully non-  
894 linear water wave modeling. In: *The Twenty-fourth International Ocean and Polar Engineering*  
895 *Conference*. International Society of Offshore and Polar Engineers; 2014. .
- 896 [22] Bai W, Eatock Taylor R. Fully nonlinear simulation of wave interaction with fixed and floating  
897 flared structures. *Ocean Engineering*. 2009;36(3):223 – 236.
- 898 [23] Ogilvie TF. Second-order hydrodynamic effects on ocean platforms. In: *Proceedings of the*  
899 *International Workshop on Ship and Platform Motions*, Berkeley; 1983. p. 205–265.
- 900 [24] Shao YL, Faltinsen OM. Towards efficient fully-nonlinear potential-flow solvers in marine hy-  
901 drodynamics. In: *ASME 2012 31st International Conference on Ocean, Offshore and Arctic*  
902 *Engineering*. American Society of Mechanical Engineers Digital Collection; 2012. p. 369–380.
- 903 [25] Wang J, Faltinsen OM, Duan W. A high-order harmonic polynomial method for solv-  
904 ing the Laplace equation with complex boundaries and its application to free-surface flows.  
905 Part I: two-dimensional cases. *International Journal for Numerical Methods in Engineering*.  
906 2020;121(17):3893–3925.
- 907 [26] Rokhlin V. Rapid solution of integral equations of classical potential theory. *Journal of compu-*  
908 *tational physics*. 1985;60(2):187–207.
- 909 [27] Fochesato C, Dias F. A fast method for nonlinear three-dimensional free-surface waves.  
910 *Proceedings of the Royal Society A: Mathematical, Physical and Engineering Sciences*.  
911 2006;462(2073):2715–2735.
- 912 [28] Hague C, Swan C. A multiple flux boundary element method applied to the description of  
913 surface water waves. *Journal of Computational Physics*. 2009;228(14):5111–5128.
- 914 [29] Grilli S, Svendsen I. Corner problems and global accuracy in the boundary element solution of  
915 nonlinear wave flows. *Engineering Analysis with Boundary Elements*. 1990;7(4):178–195.
- 916 [30] Tanizawa K. The state of the art on numerical wave tank. In: *Proceedings of 4th Osaka*  
917 *Colloquium on Seakeeping Performance of Ships 2000*; 2000. p. 95–114.
- 918 [31] Li B, Fleming CA. A three dimensional multigrid model for fully nonlinear water waves. *Coastal*  
919 *Engineering*. 1997;30(3-4):235–258.
- 920 [32] Bingham HB, Zhang H. On the accuracy of finite-difference solutions for nonlinear water waves.  
921 *Journal of Engineering Mathematics*. 2007;58(1-4):211–228.
- 922 [33] Engsig-Karup AP, Bingham HB, Lindberg O. An efficient flexible-order model for 3D nonlinear  
923 water waves. *Journal of computational physics*. 2009;228(6):2100–2118.
- 924 [34] Engsig-Karup AP, Madsen MG, Glimberg SL. A massively parallel GPU-accelerated model for  
925 analysis of fully nonlinear free surface waves. *International Journal for Numerical Methods in*  
926 *Fluids*. 2012;70(1):20–36.
- 927 [35] Ma Q, Wu G, Eatock Taylor R. Finite element simulation of fully non-linear interaction between  
928 vertical cylinders and steep waves. Part 1: methodology and numerical procedure. *International*  
929 *Journal for Numerical Methods in Fluids*. 2001;36(3):265–285.

- 930 [36] Wu G, Eatock Taylor R. The coupled finite element and boundary element analysis of nonlinear  
931 interactions between waves and bodies. *Ocean Engineering*. 2003;30(3):387–400.
- 932 [37] Wang C, Wu G. An unstructured-mesh-based finite element simulation of wave interactions  
933 with non-wall-sided bodies. *Journal of fluids and structures*. 2006;22(4):441–461.
- 934 [38] Yan S, Ma Q. Numerical simulation of fully nonlinear interaction between steep waves  
935 and 2D floating bodies using the QALE-FEM method. *Journal of Computational physics*.  
936 2007;221(2):666–692.
- 937 [39] Deeks AJ, Cheng L. Potential flow around obstacles using the scaled boundary finite-element  
938 method. *International journal for numerical methods in fluids*. 2003;41(7):721–741.
- 939 [40] Wolf JP. *The scaled boundary finite element method*. John Wiley & Sons; 2003.
- 940 [41] Li B, Cheng L, Deeks AJ. Wave diffraction by vertical cylinder using the scaled boundary finite  
941 element method. In: *World Congress on Computational Mechanics VI*. vol. 313. Beijing:[sn];  
942 2004. .
- 943 [42] Tao L, Song H, Chakrabarti S. Scaled boundary FEM solution of short-crested wave diffraction  
944 by a vertical cylinder. *Computer methods in applied mechanics and engineering*. 2007;197(1-  
945 4):232–242.
- 946 [43] Zietsman J. The coupled finite element and boundary integral analysis of ocean wave loading:  
947 A versatile tool. *Computer methods in applied mechanics and engineering*. 1984;44(2):153–176.
- 948 [44] Shao YL, Faltinsen OM. A harmonic polynomial cell (HPC) method for 3D Laplace equation  
949 with application in marine hydrodynamics. *Journal of Computational Physics*. 2014;274:312–  
950 332.
- 951 [45] Ma S, Hanssen FC, Siddiqui MA, Greco M, Faltinsen OM. Local and global properties of the  
952 harmonic polynomial cell method: In-depth analysis in two dimensions. *International Journal  
953 for Numerical Methods in Engineering*. 2018;113(4):681–718.
- 954 [46] Bardazzi A, Lugni C, Antuono M, Graziani G, Faltinsen OM. Generalized HPC method for the  
955 Poisson equation. *Journal of Computational Physics*. 2015;299:630–648.
- 956 [47] Hanssen FCW. *Non-Linear Wave-Body Interaction in Severe Waves*. Norwegian University of  
957 Science and Technology; 2019.
- 958 [48] Fredriksen AG, Kristiansen T, Faltinsen OM. Experimental and numerical investigation of wave  
959 resonance in moonpools at low forward speed. *Applied Ocean Research*. 2014;47:28–46.
- 960 [49] Hanssen FCW, Greco M, Shao Y. The harmonic polynomial cell method for moving bodies  
961 immersed in a Cartesian background grid. In: *ASME 2015 34th International Conference on  
962 Ocean, Offshore and Arctic Engineering*. American Society of Mechanical Engineers Digital  
963 Collection; 2015. .
- 964 [50] Zhu W, Greco M, Shao Y. Improved HPC method for nonlinear wave tank. *International  
965 Journal of Naval Architecture and Ocean Engineering*. 2017;9(6):598–612.
- 966 [51] Hanssen FC, Bardazzi A, Lugni C, Greco M. Free-surface tracking in 2D with the harmonic poly-  
967 nomial cell method: Two alternative strategies. *International Journal for Numerical Methods  
968 in Engineering*. 2018;113(2):311–351.
- 969 [52] Robaux F, Benoit M. Development and validation of a numerical wave tank based on the  
970 Harmonic Polynomial Cell and Immersed Boundary methods to model nonlinear wave-structure  
971 interaction. *arXiv preprint arXiv:200908937*. 2020;.
- 972 [53] Liang H, Santo H, Shao Y, Law YZ, Chan ES. Liquid sloshing in an upright circular tank under  
973 periodic and transient excitations. *Physical Review Fluids*. 2020;5(8):084801.

- 974 [54] Tong C, Shao Y, Hanssen FCW, Li Y, Xie B, Lin Z. Numerical analysis on the generation,  
975 propagation and interaction of solitary waves by a Harmonic Polynomial Cell Method. *Wave*  
976 *Motion*. 2019;88:34–56.
- 977 [55] Shen Y, Marilena G, Faltinsen OM, Ma S. Numerical study towards closed fish farms in waves  
978 using two Harmonic Polynomial Cell methods. In: *Proceedings of 35th International Workshop*  
979 *on Water Waves and Floating Bodies. The International Workshop on Water Waves and Floating*  
980 *Bodies*; 2020. .
- 981 [56] Kontos S. *Robust Numerical Methods for Nonlinear Wave-Structure Interaction in a Moving*  
982 *Frame of Reference*. Technical University of Denmark; 2016.
- 983 [57] Liu Y, Xue M, Yue DK. Computations of fully nonlinear three-dimensional wave-wave and wave-  
984 body interactions. Part 2. Nonlinear waves and forces on a body. *Journal of Fluid Mechanics*.  
985 2001;438:41.
- 986 [58] Tanizawa K. A nonlinear simulation method of 3-D body motions in waves (1st Report). *Journal*  
987 *of the Society of Naval Architects of Japan*. 1995;1995(178):179–191.
- 988 [59] Wu G. Transient motion of floating body in steep water waves. In: *Proc. 11th Workshop on*  
989 *water waves and Floating Bodies*; 1996. .
- 990 [60] Beck R. Nonlinear ship motion computations using the desingularized method. In: *Proc. 20th*  
991 *Symp. on Naval Hydrodynamics*; 1996. p. 227–246.
- 992 [61] Kashiwagi M. Non-linear simulations of wave-induced motions of a floating body by means of  
993 the mixed Eulerian-Lagrangian method. *Proceedings of the Institution of Mechanical Engineers,*  
994 *Part C: Journal of Mechanical Engineering Science*. 2000;214(6):841–855.
- 995 [62] Wu G, Hu Z. Simulation of nonlinear interactions between waves and floating bodies through  
996 a finite-element-based numerical tank. *Proceedings of the Royal Society of London Series A:*  
997 *Mathematical, Physical and Engineering Sciences*. 2004;460(2050):2797–2817.
- 998 [63] Bandyk PJ, Beck RF. The acceleration potential in fluid–body interaction problems. *Journal*  
999 *of Engineering Mathematics*. 2011;70(1-3):147–163.
- 1000 [64] Zhao R, Faltinsen O, Aarsnes J. Water entry of arbitrary two-dimensional sections with and  
1001 without flow separation. In: *Proceedings of the 21st symposium on naval hydrodynamics*; 1996.  
1002 p. 408–423.
- 1003 [65] Greco M. *A Two-dimensional Study of Green-water Loading (Ph. D. dissertation)*. Norwegian  
1004 *University of Science and Technology, Trondheim, Norwegian*; 2001.
- 1005 [66] Sun H. *A boundary element method applied to strongly nonlinear wave-body interaction prob-*  
1006 *lems*. Norwegian University of Science and Technology; 2007.
- 1007 [67] Newman JN. *Marine hydrodynamics*. The MIT Press; 2017.
- 1008 [68] Rienecker M, Fenton J. A Fourier approximation method for steady water waves. *Journal of*  
1009 *fluid mechanics*. 1981;104:119–137.
- 1010 [69] Fenton J. The numerical solution of steady water wave problems. *Computers & Geosciences*.  
1011 1988;14(3):357–368.
- 1012 [70] Clamond D, Dutykh D. Accurate fast computation of steady two-dimensional surface gravity  
1013 waves in arbitrary depth. *Journal of Fluid Mechanics*. 2018;844:491–518.
- 1014 [71] Mayer S, Garapon A, Sørensen LS. A fractional step method for unsteady free-surface flow  
1015 with applications to non-linear wave dynamics. *International Journal for Numerical Methods in*  
1016 *Fluids*. 1998;28(2):293–315.

- 1017 [72] Fuhrman DR, Madsen PA, Bingham HB. Numerical simulation of lowest-order short-crested  
1018 wave instabilities. *Journal of Fluid Mechanics*. 2006;563:415.
- 1019 [73] Chen Q, Kelly DM, Dimakopoulos AS, Zang J. Validation of the PICIN solver for 2D coastal  
1020 flows. *Coastal Engineering*. 2016;112:87–98.
- 1021 [74] Palm J, Eskilsson C, Paredes GM, Bergdahl L. Coupled mooring analysis for floating wave  
1022 energy converters using CFD: Formulation and validation. *International Journal of Marine  
1023 Energy*. 2016;16:83–99.
- 1024 [75] Savitzky A, Golay MJ. Smoothing and differentiation of data by simplified least squares proce-  
1025 dures. *Analytical chemistry*. 1964;36(8):1627–1639.
- 1026 [76] Maruo H. On the increase of the resistance of a ship in rough seas. *Journal of Zosen Kiokai*.  
1027 1960;1960(108):5–13.
- 1028 [77] Nojiri MK N. A Study on the Drifting Force on Two-Dimensional Floating Body in Regular  
1029 Waves. *Transactions of the West-Japan Society of Naval Architects*. 1975;p. 51:131–152.
- 1030 [78] Koo W. Fully nonlinear wave-body interactions by a 2D potential numerical wave tank. Texas  
1031 A&m University; 2004.
- 1032 [79] Tanizawa K, Minami M, Naito S, et al. Estimation of wave drift force by numerical wave tank.  
1033 In: *The Ninth International Offshore and Polar Engineering Conference*. International Society  
1034 of Offshore and Polar Engineers; 1999. .
- 1035 [80] Berland J, Bogey C, Marsden O, Bailly C. High-order, low dispersive and low dissipative  
1036 explicit schemes for multiple-scale and boundary problems. *Journal of Computational Physics*.  
1037 2007;224(2):637–662.
- 1038 [81] Ducrozet G, Engsig-Karup AP, Bingham HB, Ferrant P. A non-linear wave decomposition model  
1039 for efficient wave–structure interaction. Part A: Formulation, validations and analysis. *Journal  
1040 of Computational Physics*. 2014;257:863–883.
- 1041 [82] Tasai F, Koterayama W. Nonlinear hydrodynamic forces acting on cylinders heaving on the  
1042 surface of a fluid. *Rep Res Inst Appl Mech Kyushu Univ*. 1976;24:1–39.
- 1043 [83] Grytøyr G. A higher-order boundary element method and applications to marine hydrodynam-  
1044 ics. Norwegian University of Science and Technology, Trondheim, Norwegian; 2008.
- 1045 [84] Wang J, Faltinsen OM. A harmonic polynomial method based on Cartesian grids with local  
1046 refinement for complex wave-body interactions. In: *Proceedings of 33rd International Workshop  
1047 on Water Waves and Floating Bodies*. The International Workshop on Water Waves and Floating  
1048 Bodies; 2018. .